Lightweight and Compact Radiometers for Soil Moisture Measurement

A review

©SHUTTERSTOCK.COM/TARASVYSHNYA

TRONG KHOA HO, JIEWEI FENG, FARAH BILAWAL, SHAHRIAR HASAN SHEHAB, KIM TUYEN TRINH, YANG YANG, CHRISTOPH RÜDIGER, JEFFREY P. WALKER, AND NEMAI CHANDRA KARMAKAR

Fresh water is considered to be one of the most precious natural resources in many countries. Given that soil moisture plays a salient role in vegetation growth, the continuous and timely measurement of soil moisture content is critical to manage water shortages, especially in the agriculture sector [1], [2], which is the largest water use sector in Australia. A 10% water savings in the Australian agriculture sector would be equivalent to a reduction of more than 30% of the combined water consumption from Australian

Digital Object Identifier 10.1109/MGRS.2021.3082179
Date of current version: 29 June 2021

capital cities [3]. Further, soil moisture influences the process of rainfall being partitioned into runoff and infiltration, and saturated soil could turn heavy rain into floods. Therefore, soil moisture information is essential for accurate climate forecasting as well as improving flood and drought prediction [3]–[5].

Like all materials, soil has unique physical properties. It emits a different level of thermal radiation depending on its physical temperature and the ratio of soil particles, water, and air content present. These thermal radiations are, therefore, related to the emissivity of the soil through the dielectric constant of the soil–water–air mixture [6], [7].

Researchers have devoted a substantial amount of time to developing microwave remote sensing systems to monitor the moisture content present in soil [8]–[11]. Microwave frequencies, instead of optical or other bands, are promising because they are less sensitive to solar illumination, vegetation canopy, and weather conditions [12]. Therefore, microwave sensing can be conducted at any time of the day or night. Further, microwave sensing is directly related to the water content of soil via the soil dielectric constant [4].

SOIL EMITS A DIFFERENT LEVEL OF THERMAL RADIATION DEPENDING ON ITS PHYSICAL TEMPERATURE AND THE RATIO OF SOIL PARTICLES, WATER, AND AIR CONTENT PRESENT.

Microwave moisture measurements can be undertaken in two different ways: passive and active sensing. The difference between passive and active measurements is that passive measurements consist of natural microwave emissions from objects or surfaces, which are then observed by a radiometer system through the measurement of a "brightness temperature." Based on the brightness temperature value, the moisture content of the soil is derived [13], [15]. Conversely, active measurements are undertaken by radars in which microwave pulses are sent to a target and then received back after scattering. The backscattered energy is then measured and used to relate the properties of the soil, including the surface roughness, vegetation, and moisture content [15], [16].

These two microwave sensing techniques offer very different resolutions. Active microwave sensing can offer a spatial resolution lower than 100 m using synthetic aperture processing, while passive sensing gives a coarse resolution greater than 10 km from satellite altitudes. Even though the active sensor has a higher resolution, the scattering from Earth's surface is more difficult to interpret than the naturally emitted signals [17]. This explains why microwave active sensors do not provide as accurate measurement of soil moisture as microwave radiometers [4], [17].

A few contemporary microwave radiometers that have been successfully launched into space are the *Advanced Microwave Scanning Radiometer 2* (*AMSR-2*), *Soil Moisture and Ocean Salinity* (*SMOS*) radiometer, *Fengyun-3B* microwave radiation imager, *Aquarius* radiometer, and, most recently, *Soil Moisture Active and Passive* (*SMAP*) instrument [19]. These radiometers provide global measurements at frequencies ranging from the L to E bands.

However, operating frequencies lower than the X band, especially in the L band, are most suitable for soil moisture retrieval studies compared to higher-frequency bands, because of their increased penetration depth, greater sensitivity to the dielectric constant of wet soil, and less severe vegetation-masking effect [15], [19].

Apart from soil moisture sensing, the L band is also promising for other environmental sensing applications. By utilizing the protected 27-MHz bandwidth at the L band (1,400–1,427 MHz) [20] and its higher sensitivity of brightness temperature to sea surface salinity (SSS) compared to that of higher-frequency bands, both the *SMOS* and *Aquarius* radiometers provided coarse resolution and long revisit/averaging time but high-precision radiometric measurements for SSS monitoring [on the order of 0.2 practical salinity units(psu)] [20], [21]. *SMAP* has also been able to provide eight-day and monthly SSS data by adapting the *Aquarius*'s salinity retrieval algorithm. Among these three sensors, *Aquarius* had the most accurate SSS swath product (but lower native spatial resolution), while *SMAP* data were the least affected by radio-frequency interference (RFI) [20]. Since the contrast in dielectric constants between water and ice is larger at the L band than at other higher-frequency bands [22], all three radiometers have been able to generate level 3 freeze/thaw information [23]–[25]. Additionally, level 3 wind speed data are available from *SMAP* and *SMOS* with the distinctive advantage of L-band sensitivity being less affected by rain and severe wind [26]–[28]. In addition, because of its unique capability to accurately measure thin ice coverage [29], *SMOS* also provides level 3 sea ice thickness data [30].

Apart from obtaining accurate measurements, another critical consideration for airborne and spaceborne systems is reducing the payload's weight. The price to deliver a kilogram of payload to low-Earth orbit (LEO) varies from approximately US$1,500 to more than US$20,000, depending on the spacecraft [31]. Engineering a compact and lightweight yet accurate radiometer system is undoubtedly a must in the future.

The design of such a lightweight and accurate radiometer system requires several aspects to be considered, including the tradeoff between the antenna aperture size and spatial resolution as well as the techniques used to obtain multiangular measurements and their tradeoffs in terms of system size and performance. To the best of the authors' knowledge, these aspects of a radiometer system have not been comprehensively reviewed. Hence, this article first discusses current satellite radiometers and further explores methods to realize a lightweight, compact, and cost-saving radiometer for soil moisture remote sensing.

THE *SMOS* AND *SMAP* MISSIONS

SMAP is a NASA mission developed within the Earth System Science *Pathfinder* program. Its goal is to measure and collect soil moisture data with global coverage in a short revisit time, helping scientists to monitor and characterize the relationship between soil moisture and its freeze/thaw state as well as their effects on the global ecosystem [32]. Similarly, *SMOS* was proposed to the Earth Explorer *Opportunity* missions issued by the European Space Agency (ESA) in 1998, with the aim of providing scientists with information about soil moisture and SSS on a global scale [33]. These data are vital for predicting environmental hazards, such as droughts, floods, and bush fires, as well as improving agricultural activities, such as crop planning, by providing information on water availability and environmental stress [17].

The *SMAP* instrument featured a conically scanning real-aperture antenna with a combined polarimetric L-band radar and radiometer and is hence known as an active/passive mission. However, the radar stopped working in July 2015 due to the malfunctioning of its high-power amplifier [44]. In contrast, the *SMOS* mission has a 2D synthetic aperture L-band radiometer [the Microwave Imaging Radiometer by Aperture Synthesis (MIRAS)] operating within the protected band (1,400–1,427 MHz) [17], [33].

A fixed-angle, real-aperture antenna, like the one used in *SMAP*, requires scanning either electrically or mechanically to cover a wide swath, which is essential to meet the revisit time requirement. Alternatively, multiangular or multibeam antennas (obtained from either signal processing techniques, such as the aperture-synthesis [33]–[35] and digital beam-forming (DBF) techniques [36], or complex real-aperture antenna systems [34]) allow simultaneous observations of multiple footprints at different incidence angles covering a wide swath [34], [35]. Hence, scanning is not necessary in such systems. Since both horizontal (H)- and vertical (V)-polarized waves can be observed by the *SMAP* and *SMOS* instruments, the four Stokes parameters can be derived. The scientific requirements of *SMAP* and *SMOS* can be viewed in Table 1.

ANTENNAS

The antenna used for the *SMAP* instrument is an offset-fed, deployable parabolic reflector antenna that has the capability of receiving and transmitting both H- and V-polarized electromagnetic waves [37]. The reflector boom assembly (RBA) is mechanically rotated around the vertical axis to change the field of view (FOV). This gives the *SMAP* instrument the ability to scan a wide area while it is orbiting Earth. Due to the resolution requirements, a relatively large antenna must be used. Consequently, the RBA has a diameter of 6 m and is shared by both the radar and radiometer. Beam efficiency, reflector surface emissivity, and temperature are the main drivers for the antenna to achieve accurate radiometric measurement results [37].

In contrast, the SMOS instrument known as *MIRAS* utilizes 69 antenna elements equally spaced (0.875λ) along Y-shaped arms for its antenna system [17], [41]. This antenna configuration grants MIRAS the ability to capture brightness temperature maps from Earth over a range of incidence angles (0–55°) across a swath of approximately 1,000 km with a spatial resolution of 35–50 km [41] (Table 2). The aperture-synthesis approach relaxes the stringent requirements on the performance of the antennas, but the system sensitivity is reduced by a factor of approximately 1.5–2 (depending on the aperture-synthesis configuration) as compared to those of real-aperture radiometers [42]. The key parameters of the *SMAP* and *SMOS* antenna elements are summarized in Table 3.

RFI MITIGATION

Since the *SMAP* and *SMOS* instruments measure the brightness temperature over land areas, they are prone to heavy interference from radio activities [43]–[45]. Even though the radiometer is operating within the strictly protected band (1,400–1,427 MHz) for a scientific space observatory,

TABLE 1. THE SMAP AND SMOS SCIENTIFIC REQUIREMENTS, BASED ON [17] AND [38].

PARAMETER	*SMAP*	*SMOS*
Accuracy	*Soil moisture*: ±0.04 $m^3 \cdot m^{-3}$ volumetric accuracy in the top 2–5 cm for vegetation water content of <5 $kg \cdot m^{-2}$ *Freeze/thaw state*: capture the freeze/thaw state transitions in an integrated vegetation–soil continuum with two-day precision at the spatial scale of landscape variability (~3 km)*	*Soil moisture*: ±0.04 $m^3 \cdot m^{-3}$ volumetric accuracy *Vegetation water content*: 0.1 $kg \cdot m^{-2}$ *SSS*: 0.1–0.2 pss-78**
Spatial resolution	*Hydrometeorology*: ~10 km *Hydroclimatology*: ~40 km	*Soil moisture*: <50 km *Vegetation water content*: <50 km *SSS*: 100–200 km
Revisit time	Sample diurnal cycle at consistent time of day (6 and 18 h) *Global*: ~three-day revisit *Boreal*: ~two-day revisit	*Soil moisture*: <three days *Vegetation water content*: <five days *SSS*: 10–30 days

*The 3-km-resolution freeze/thaw state product was planned to be acquired by the radar of *SMAP*. Due to the malfunction of this radar in July 2015, the 3-km high-resolution data cover only a limited time frame (of 12 weeks). As an alternative, a freeze/thaw state product has been developed from the *SMAP* radiometer measurements with an enhanced resolution of 9 km [39], [40].
**pss-78 is a salinity unit according to the Practical Salinity Scale of 1978 [17].

according to the International Telecommunication Union–Radiocommunication (ITU-R) Sector Radio Regulation footnote 5.340 [46], strong RFI was still observed due to unauthorized, cheap, or malfunctioning sources on Earth [37], [46]–[48]. The RFI power biases the radiometric measurements, leading to erroneous results. While moderate to strong RFI power (>40 K) can be detected and discarded, causing data loss, small RFI power is more difficult to detect and greatly impacts the accuracy of results [44], [46]. Figure 1 shows several RFI sources detected in Central Europe in October 2010 [46].

Realizing the detrimental effects that these RFI sources have on the accuracy of the collected scientific data, the ESA has been detecting and reporting RFI sources to the National Spectrum Management authorities and requesting them to investigate and switch off these unauthorized or faulty sources [46]. In parallel, the ESA is also working on new RFI mitigation algorithms for future applications [46]. Since NASA was aware of this situation during its mission design, it adopted RFI mitigation techniques in its measurements and ground-processing software [37], [44].

There are two main types of RFI sources: pulsed and narrowband [e.g., continuous-wave (CW)-like] signals [45]. Pulsed-signal RFI can be corrected using time-domain pulse thresholding if the radiometer is sampled at a sufficiently high temporal resolution. For CW signals, the *SMAP* radiometer's bandwidth is subdivided into 16 × 1.5-MHz subbands using a digital filter [45]. This allows a spectrogram of 1.5-MHz × 1-ms resolution to be created. Then, RFI detection methods such as channelized pulse detection, cross-frequency, kurtosis, and polarization–anomaly detection algorithms [37], [45], [49] can be applied.

Figure 2 shows global maps of soil moisture retrieved by the *SMOS* instrument and the vertical-polarized single-channel algorithm of *SMAP* over a one-week period from 1 June 2015 to 7 June 2015. These two maps show the expected spatial patterns of soil moisture. However, dense vegetation and low to moderate RFI contamination are the main sources of different retrieval results between the two missions [50].

TABLE 2. THE MIRAS INSTRUMENT KEY PARAMETERS SUMMARY, ADOPTED FROM [41] AND [52].

Operating frequency	1.413 GHz (L band)
Integration time	1.2 s
Measurement modes	Dual polarized or full polarized
For radiometric measurements over land	
Spatial resolution	30–50 km
Estimated sensitivity	3.5 K (B)* and 5.8 K (E)**
For radiometric measurements over ocean	
Spatial resolution	50 km after an overpass
Estimated sensitivity	2.5 K (B)* and 4.1 K (E)**

*B stands for boresight.
**E stands for edge of swath.

TABLE 3. THE *SMAP* AND *SMOS* ANTENNA KEY PARAMETERS, BASED ON [37], [43], AND [44].

***SMAP* ANTENNA**	
Antenna type	Offset-fed, deployable parabolic reflector
Projected aperture	6 m
Beamwidth (3 dB)	2.7°
Swath width	1,000 km
Look and incidence angles	35.5° and 40.0°, respectively
Peak gain	36 dBi
Rotation rate	14.6 r/min
Feed type	Waveguide feed and orthogonal mode transducer (WR-650)
***SMOS* ANTENNA ELEMENT**	
Antenna type	Patch antenna without dielectric substrate
Number of antenna elements	69
Number of antenna arms and antenna arm length	3 and ~4 m, respectively
Cross-polarization ratio	>25 dB
Single-element antenna gain	~8 dBi
Single-element antenna beamwidth (3 dB)	~70°
Swath width	900 km
Incidence angles	0°–55°

RADIOMETER ELECTRONICS DESIGN

The *SMAP* radiometer is a superheterodyne receiver that consists of the following components [51]:

- *Radiometer front end*: This consists of an RF cable-based feed network; a frequency diplexer to separate the active and passive bands; and electronic front end, which is in charge of RF filtering and amplifying the input signal.

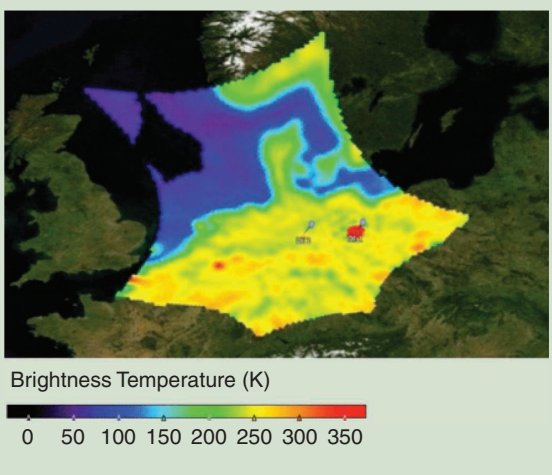

FIGURE 1. An *SMOS* snapshot showing several RFI emissions detected in Central Europe in October 2010. (Source: [46].)

Internal calibration is also available using RF switches and a common noise source.

- *RF back end*: This subnetwork is in charge of downconverting the RF signals (at 1,413 MHz) for both polarizations to an intermediate frequency (IF) of 120 MHz.
- *Radiometer digital electronics*: This subnetwork samples the downconverted IF signal to a digital signal for processing. It also performs additional filtering, subband channelization, cross correlation for measuring the third and fourth Stokes parameters, and the detection and integration of the first four raw moments of the signals. Subsequently, the data are packaged and sent to ground receiving stations for calibration and further processing.

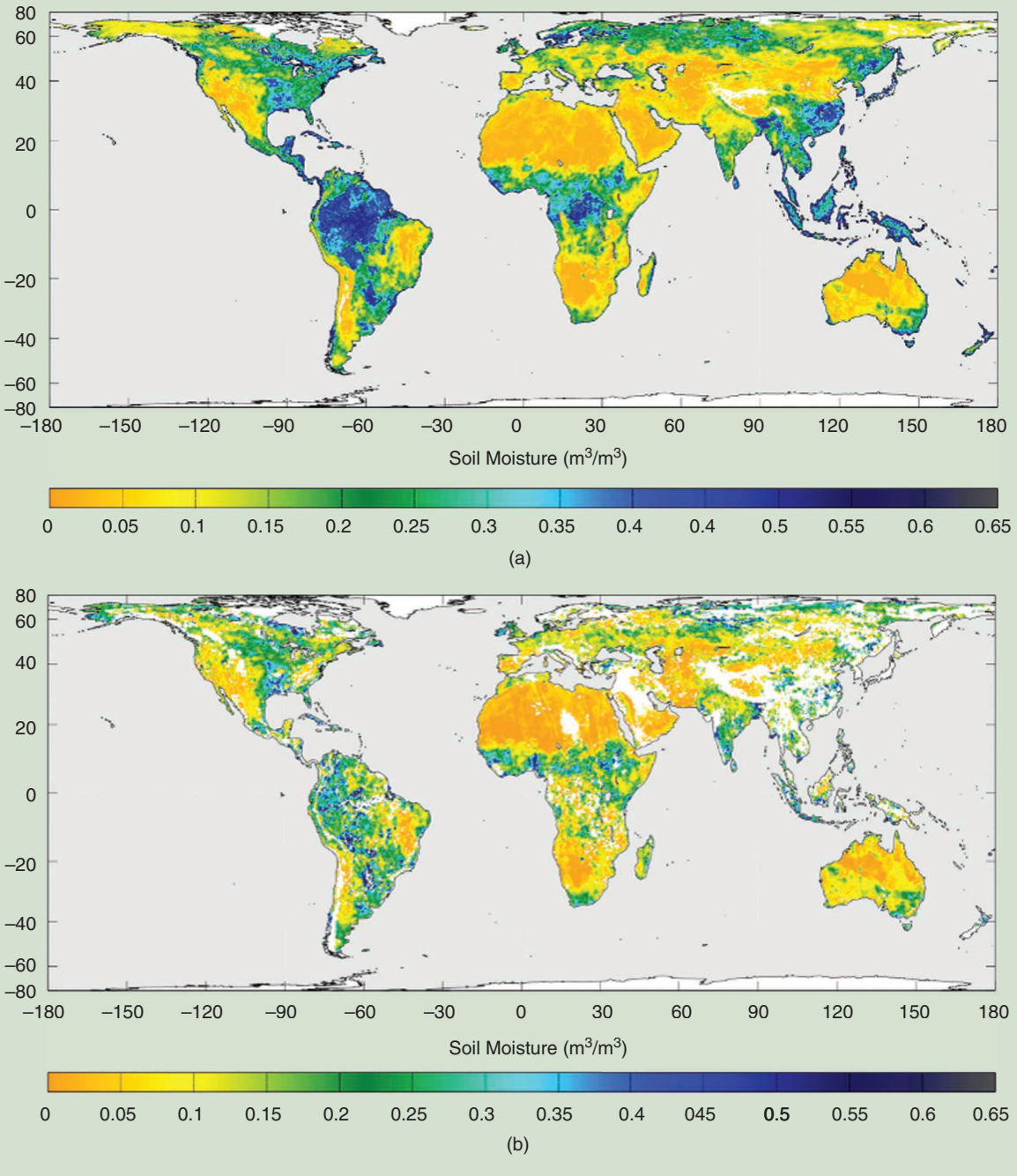

FIGURE 2. The global patterns of soil moisture retrieved by (a) the *SMAP* vertical-polarized, single-channel algorithm and (b) *SMOS* over a one-week period from 1 June 2015 to 7 June 2015. The white areas show regions of inaccurately retrieved data due to RFI and/or surface conditions, such as frozen ground, mountainous terrain, and excessive vegetation. (Source: [50].)

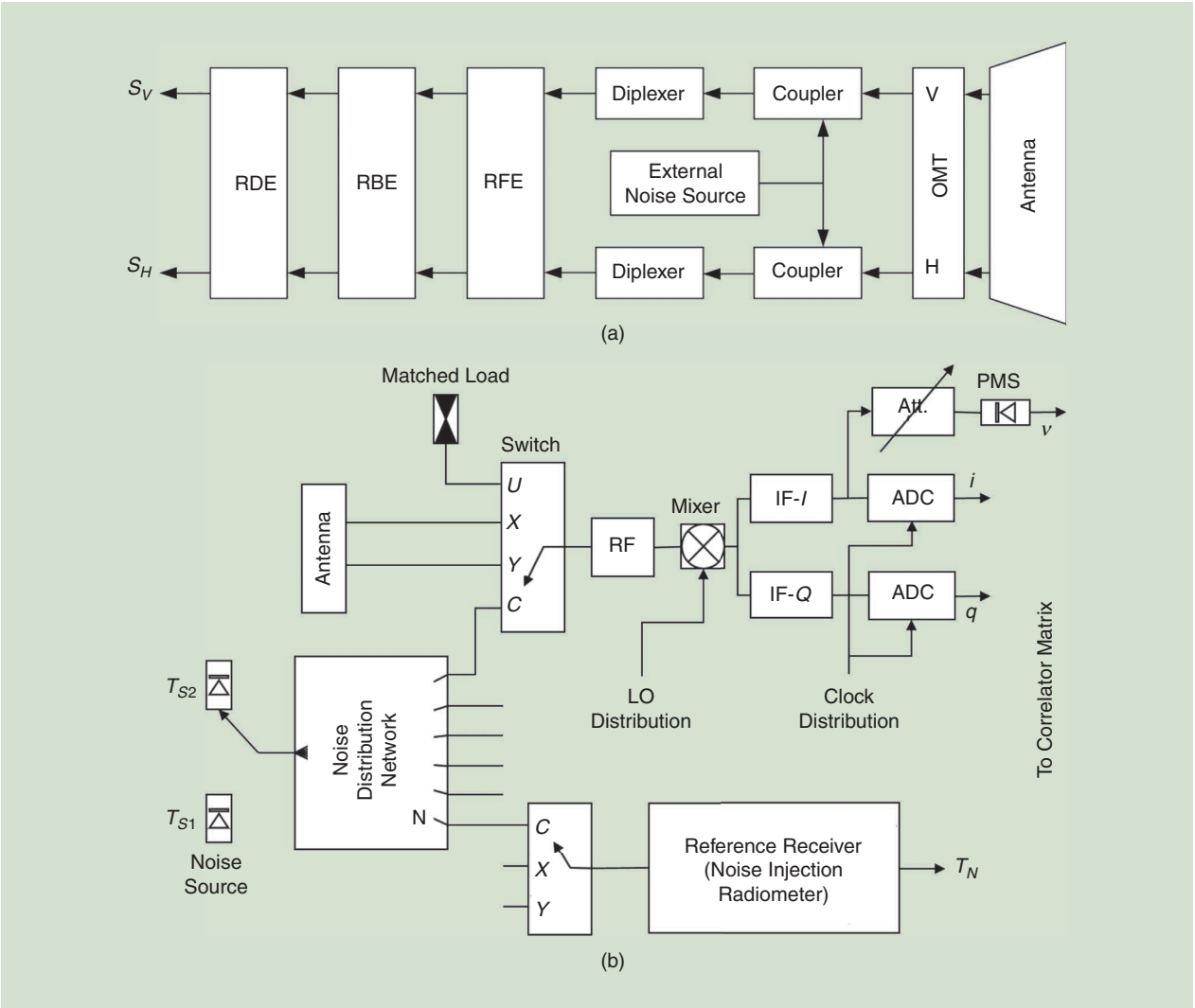

FIGURE 3. (a) An *SMAP* radiometer block diagram showing the signal paths and frequency plan. (Source: [51].) (b) A simplified LICEF block diagram along with part of the calibration hardware. (Source: [56].) ADC: analog-to-digital converter; ATT: attenuator; I: in-phase; LICEF: lightweight cost-effective front end; LO: local oscillator; OMT: object modeling technique; PMS: power measurement sensor; Q: quadrature; RBE: RF back end; RDE: radiometer digital electronics; RFE: radiometer front end.

A block diagram of the *SMAP* instrument's electronic system design is shown in Figure 3(a), with the key parameters summarized in Table 4. *SMOS* comprises 66 radiometers, which are known as *lightweight cost-effective front ends* (LICEFs), and three noise-injection radiometers (NIRs) [52]. However, each injection radiometer includes 2 LICEF receivers, making LICEF the basic receiver units in MIRAS. The three NIRs are used to measure the average antenna temperature and two noise levels of the calibration network [53]. Each LICEF generates 1-bit digital signals, which correspond to the sign of the in-phase and quadrature components of the received noise. These data are then transferred to the digital correlator by optical links [53]. The block diagram of an LICEF receiver is shown in Figure 3(b), with a detailed explanation of each component block provided in [53].

TABLE 4. THE *SMAP* INSTRUMENT KEY PARAMETERS SUMMARY, BASED ON [51].

KEY PARAMETERS OF THE RADIOMETER	
Center frequency	1.41 GHz (L band)
Resolution (root footprint area)	40 km
Channels	T_v, T_h, T_3, and T_4
Bandwidth and integration time	22 MHz and 65 ms, respectively
Estimated radiometric resolution/sensitivity	1.1 K (over land) and 0.8 K (over ocean)

COMMON TOPOLOGIES FOR RADIOMETERS

TOTAL POWER RADIOMETER

The total power radiometer (TPR) is probably the most straightforward structure for a remote sensing radiometer. In the analog domain, the input noise signal (after

being properly amplified and filtered) is passed through a diode detector circuit. Usually, diodes are operated in either the linear region or square-law region, depending on the input power [54]. However, in this particular case, it is often preferred to operate the diode detector circuit in its square-law region so that the output dc voltage will be proportional to the input noise power. Next, the detected signal is smoothed by an integrator, with the degree of smoothing dependent on the duration of the integration time. This also affects the sensitivity, in kelvin, of the radiometer through [34]

$$\Delta T = \frac{T_A + T_N}{\sqrt{B \cdot \tau}}, \tag{1}$$

where T_A and T_N are the antenna's temperature and equivalent receiver noise temperature measured in kelvin, respectively; B is the bandwidth of the input noise signal in hertz; and τ is the integration time in seconds.

The output voltage is proportional to the measured brightness temperature, which can be expressed as follows [34]:

$$V_{out} = c \cdot (T_A + T_N) \cdot G, \tag{2}$$

where V_{out} is the output voltage of the receiver measured in volts, c is a constant, and G is the system gain. The TPR exhibits the advantage of having a simple configuration, but it is susceptible to gain variation and system noise temperature, making it undesirable and even impractical in some applications. Therefore, frequent calibrations are required for the TPR to compensate for system fluctuations, which results in a reduction of the amount of time available for actual measurements.

DICKE RADIOMETER

The Dicke radiometer [55], named after R.H. Dicke, aims to reduce the dependency of the radiometer's output on the system noise temperature fluctuation by rapidly switching between observing the target brightness temperature and a known reference temperature T_R in kelvin. The output voltage of the Dicke radiometer is dependent on the difference between the antenna temperature and the known reference temperature, expressed as [34]

$$V_{out} = c \cdot (T_A - T_R) \cdot G. \tag{3}$$

Even though the output is still dependent on the system gain, its stability is greatly improved by eliminating the dependency on the system noise temperature. However, this comes at a cost: the sensitivity is twice as much (for a 50% duty cycle) compared to the sensitivity of the TPR, according to the following equation:

$$\Delta T = 2 \cdot \frac{T_A + T_N}{\sqrt{B \cdot \tau}}. \tag{4}$$

NIR

The NIR can achieve independency of the system gain and noise temperature by adding a feedback loop onto the Dicke radiometer. The objective of the NIR is to maintain a zero or near-zero voltage at the output of the Dicke radiometer through an injection of a known variable noise source. Therefore, the antenna temperature can be determined by [34]

$$T_A = (T_R - T_I), \tag{5}$$

where T_I is the output brightness temperature in kelvin of the variable noise source. From (5), it can be seen that the accuracy of the NIR is dependent on the accuracy of the Dicke reference temperature and variable noise output. These can be made stable in practice. The sensitivity of the NIR is close to that of the Dicke radiometer and can be expressed as follows [34]:

$$\Delta T = 2 \cdot \frac{T_R + T_N}{\sqrt{B \cdot \tau}}. \tag{6}$$

There are three NIR units in MIRAS [43], which are used for absolute calibration and as reference sources for the measured outputs. Since the NIR has more complexity compared to the Dicke radiometer and TPR, it poses challenges for scalability, especially for multichannel radiometers.

CORRELATION RADIOMETER

The correlation radiometer is a multichannel radiometer that measures the input noise power of each channel as well as the correlation between them. The channels can have different polarizations, as in a polarimetric radiometer. Both the MIRAS instrument for *SMOS* [57] and the *SMAP* instrument [44] utilize a polarimetric radiometer to measure the soil (and ocean) brightness temperature. Stokes parameters can be derived by cross-correlating the H- and V-polarized measured input signals based on the Rayleigh–Jeans approximation [58]:

$$T = \begin{bmatrix} T_v \\ T_h \\ T_3 \\ T_4 \end{bmatrix} = \frac{\lambda^2}{k_B \eta B} \begin{bmatrix} \langle |E_v^2| \rangle \\ \langle |E_h^2| \rangle \\ 2 \cdot R(\langle E_v E_h^* \rangle) \\ 2 \cdot \mathrm{Im}(\langle E_v E_h^* \rangle) \end{bmatrix}, \tag{7}$$

where T_h, T_v, T_3, and T_4 are the brightness temperature in kelvin of the horizontally and vertically polarized waves and the third and fourth Stokes parameters, respectively; λ is the wavelength in meters; k_B is the Boltzmann's constant; η is the impedance of the propagating medium in ohms; B is the bandwidth in hertz; E_v and E_h are the vertically and horizontally polarized electric fields in volts per meter, respectively; and $\langle . \rangle$ represents the infinite time average. The components, which constitute a

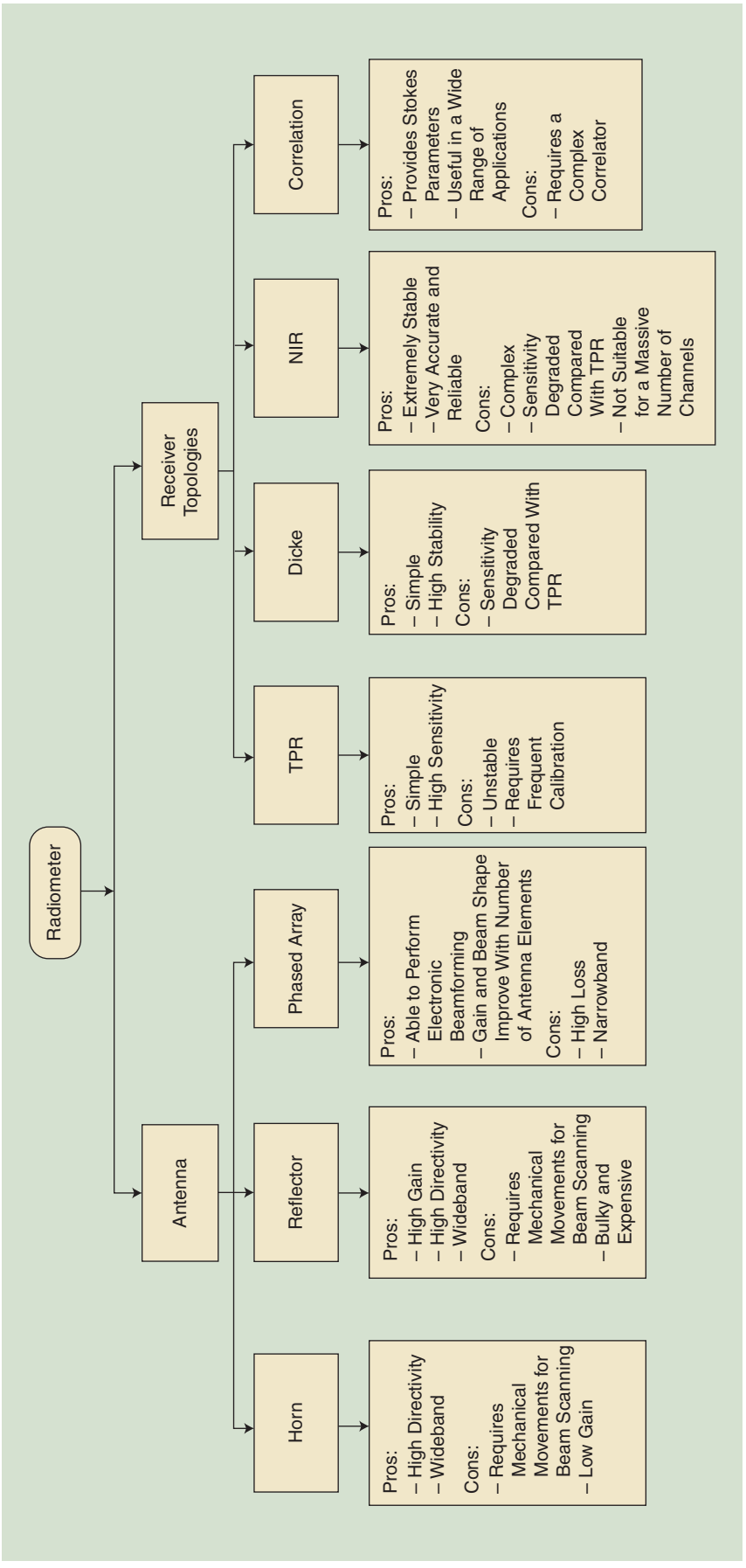

FIGURE 4. The different antenna configurations and receiver topologies for radiometers and their salient characteristics.

radiometer, are summarized in terms of their strengths and limitations in Figure 4.

DIGITAL RADIOMETERS

In analog radiometers, a square-law device, such as a diode, is used to convert the ac power of the measured brightness temperature to a corresponding dc power. This dc signal is then fed to an analog integrator before it is digitized for further processing. Conversely, a digital radiometer uses high-speed analog-to-digital converters (ADCs) to sample the ac waveform of the measured brightness temperature and then performs square-law detection and integration in a computer. Due to this, the digital radiometer can fully exploit the stability, flexibility, and convenience of digital processing [59].

Digital radiometers are very effective in detecting and mitigating RFI for soil moisture measurements, as demonstrated by the *SMAP* instrument [45]. Furthermore, DBF techniques can be used together with a multichannel digital radiometer to realize electronically steerable antennas.

Analog radiometers can be considered a special type of digital radiometer when the sampling interval reaches zero and the number of bits approaches infinity. This means that the digital detector will introduce some error into the measurements due to its finite sampling frequency and quantization. The degradation factor for a digital TPR, ignoring the quantization effect, can be presented as follows [59]:

$$F^2 = B_{\mathrm{E}}\Delta + 2B_{\mathrm{E}}\Delta \sum_{k=1}^{\infty} \left[\frac{R_{x_c}(k\Delta)}{\sigma^2_{x_c}} \right]^2, \tag{8}$$

where F represents the degradation of the sensitivity of a digital compared to an analog TPR, $R_x(\mu)$ is the autocorrelation function of the process $x(t)$, $x_c(t)$ is the in-phase analog component of the signal, σ_{x_c} is the standard

deviation of $x_c(t)$, and B_E is the effective bandwidth of the system. $R_{x_c}(\mu)$ can be expressed as [59]

$$R_{x_c}(\mu) = 2\int_0^\infty S_x(f)\cos[2\pi(f-f_0)\mu]\,df, \tag{9}$$

where $S_x(f)$ is the power spectral density of $x(t) = x_c(t)\cos(2\pi f_0 t) - x_s(t)\sin(2\pi f_0 t)$, $x_s(t)$ is the quadrature analog component of the signal, and f_0 is the IF frequency.

In (8) and (9), it is assumed that the system frequency response $H_0(f)$ has a bandpass shape and is symmetric about f_0. Hence, depending on the bandpass filter topology used in the system, the degradation factor will have different values. In [59], several common bandpass shapes have been used to calculate the degradation factor. It is observed that, when the sampling rate is greater than the Nyquist rate, the degradation factor is equal to one. However, when the quantization effect is considered along with the finite sampling rate, the degradation factor (assuming that the sampling rate is not too fast, the step size of the quantizer is small compared to the standard deviation of the process $x_c(t)$, and no saturation occurs) can be approximated as the following equation [59]:

$$F^2 = F_{NQ}^2 + \frac{1}{6}\frac{a^2}{\sigma_{x_c}^2}B_E\Delta + \frac{1}{360}\frac{a^4}{\sigma_{x_c}^4}B_E\Delta, \tag{10}$$

where F_{NQ} is the degradation factor in (8), and a is the quantizer step size. The numerical results in [59] show that, for a normalized root mean square (RMS) value of σ_x/L, where L is the saturation level of the quantizer, equal to around 0.35, and the number of the quantization level is $N > 4$ (>2 bits), the degradation factor is the lowest.

Comparisons of the degradation factors calculated using (10) and the exact results from [59] are shown in Figure 5. As stated in [59], (10) works reliably only when the sampling interval is not too small, the step size a is small with respect to σ_x, and, most importantly, no saturation occurs in the quantizer. This is clearly shown in Figure 5(a) and (c). As σ_x/L increases from 0.2 to 1.5, the degradation factor approaches the ideal curve of no quantization error. However, when σ_x/L reaches 0.6 and above, the quantization error starts to rise due to saturation. This is totally opposite to Figure 5(a), where the curve for $\sigma_x/L = 0.6, 1.0$, and 1.5 almost overlays the ideal curve.

Additionally, the quantizer error of $\sigma_x/L = 0.2$ is greater than that of $\sigma_x/L = 0.4$ due to the second condition mentioned above. Overall, the approximation seems to give the most reliable results for $\sigma_x/L = 0.4$ [Figure 5(b)], as also stated in [59].

A performance analysis of an L-band radiometer with DBF [the Passive Advanced Unit Radiometer (PAU-RAD)] has been presented in [60] using the noise waves technique. Since PAU-RAD uses a Wilkinson power divider to modify the original TPR output to be similar to that of the Dicke radiometer topology, where the reference noise signal of the Dicke load is replaced with one of the Wilkinson power divider resistances, the sensitivity of each channel is found to be increased by $2 * T_{ph}$, where T_{ph} is the physical temperature of the components.

Additionally, the impacts of the number of bits and input noise levels have been investigated for the PAU-RAD system in [61]. Using simulations, the researchers found that ADCs with a resolution of 8 bits and above as well as an input voltage range of $V_{p-p} = 9.09\sigma_{SIGNAL}$ produced results with negligible errors compared to those of an analog radiometer.

A digital radiometer allows complex digital signal processing algorithms to be applied in the postprocessing stage

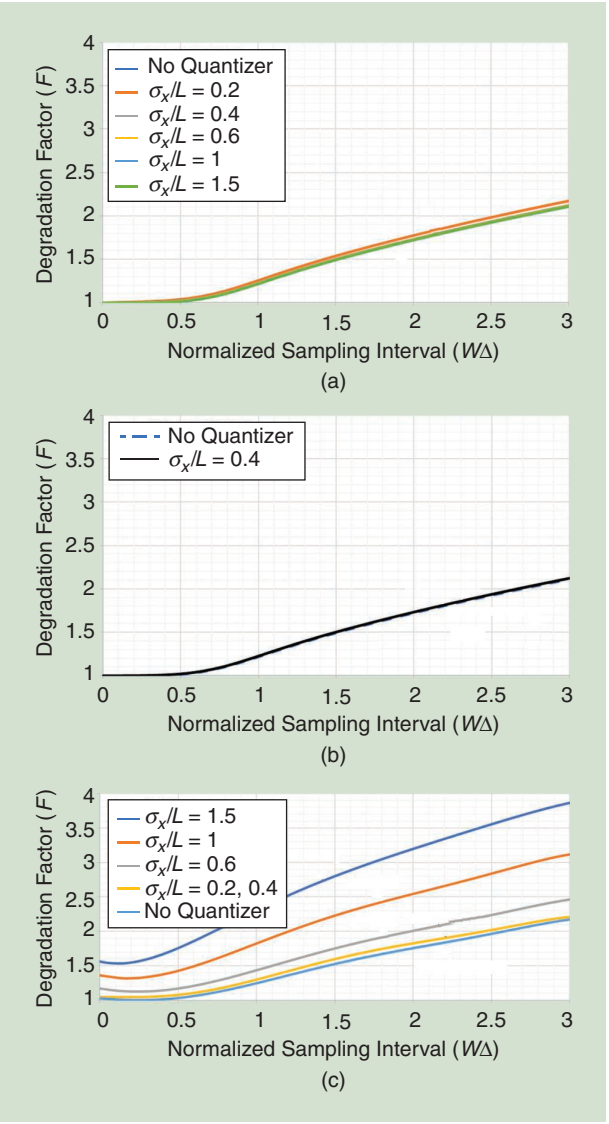

FIGURE 5. A comparison of the degradation factors approximated using (10) and the exact results from [59] for the Gaussian and Butterworth filter response and number of quantization level equal to 17. (a) The degradation factors approximated using (10) for "no quantization error" and $\sigma_x/L = 0.2$, 0.4, 0.6, 1.0, and 1.5. (b) The degradation factors approximated using (10) for "no quantization error" and $\sigma_x/L = 0.4$. (c) The exact results obtained from [59].

to improve measurement accuracy [44], [62], [63]. A good example is the RFI mitigation described in "RFI Mitigation" section. Furthermore, with the development of modern ADC and digital circuits, unstable and complex analog components (RF mixers, oscillators, and so on) can be reduced by using a fast ADC and subharmonic sampling technique [64], [65] to simultaneously sample and downconvert the RF signal to a digital baseband signal for calculation.

ELECTRONIC BEAM SCANNING

In practice, there are three main techniques to perform scanning, which is required to obtain a wide swath width: the mechanical, aperture-synthesis, and electronic beam-forming approaches. The mechanical approach was used in the *SMAP* instrument to rotate the parabolic reflector for scanning Earth at a fixed incident angle [32]. The aperture-synthesis approach was utilized in the *SMOS* radiometer [52] and the Electronically Steered Thinned Aperture Radiometer [35], [66] to reconstruct the image, including pixels in the entire FOV, using signal processing [34], [67].

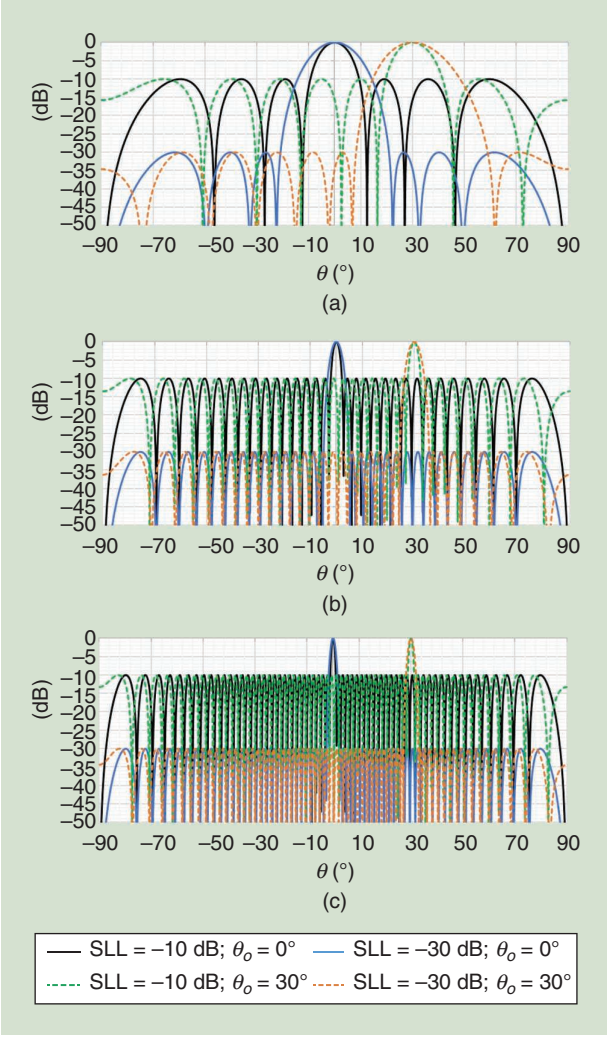

FIGURE 6. The normalized array factor of an L-band (a) 8 × 8, (b) 32 × 32, and (c) 64 × 64 Chebyshev array, all with element spacing of 0.5λ. The main beam of each synthesized array is steered to θ_0 = 0° and θ_0 = 30°, and the SLL is designed to be –10 and –30 dB, respectively.

Electronic beam-forming techniques utilize the phase information of the signals arriving at each antenna element in the array to add the received signals constructively (either in the analog or digital domains) in a given direction, hence forming a beam in that direction. This technique has been utilized in several radiometers, such as the S-194 [68], PAU-RAD [60], and Multichannel Passive Imaging Radiometer Using the DBF Technique [69].

For low-operating frequency bands, such as the L band, to achieve low beamwidth and sidelobe levels (SLLs), the antenna aperture needs to be larger than 15 m for a spatial resolution of 10 km from LEO with an altitude of 800 km [67], which is difficult to realize. Furthermore, a bigger antenna means a heavier payload, which translates into more expense during operation, especially for spaceborne and airborne radiometry applications.

In addition, mechanically steering an antenna requires mechanical moving parts and their control units, which contributes to the weight and complexity of the system. It is worth mentioning that *SMAP* has a total antenna weight of 79 kg (including a single horn and RBA), while the spin subsystem adds another 41 kg, which is more than half of the antenna weight [70]. Therefore, the synthetic aperture and electronic beam-forming techniques are beneficial to airborne and spaceborne missions operating at low-frequency bands. However, the synthetic aperture technique reduces the system sensitivity as a tradeoff [17], [34], [67]. Hence, a combination of antenna arrays and electronic beam-forming techniques that creates agile beams [36] is a strong candidate for future radiometers.

A comparative study of different power distribution methods for array-antenna beam forming for a soil moisture radiometer has been conducted in [71]. Chebyshev arrays of 8 × 8, 32 × 32, and 64 × 64 have been designed and simulated in MATLAB software. The normalized array factor with different designed SLLs and the main beam-steering angles are provided in Figure 6. The Chebyshev beam-shaping method is famous for its capability in controlling both the main lobe level and SLLs [72]. The weighting coefficients are calculated, following the procedure described in [73].

For an accurate measurement of scene brightness temperature, a radiometer system has stringent requirements on antenna beam efficiency, usually better than 90% [74]. Given that an antenna measures the brightness temperature in every direction via its main lobe and side/back lobes, a beam efficiency of >90% means that at least 90% of the total measured radiation is contributed by the main lobe of the antenna. This requires a very low antenna SLL (i.e., down to –20 to –40 dB or even lower, depending on the antenna type and array configuration); generally, a lower SLL leads to higher beam efficiencies.

However, as a tradeoff indicated in Figure 6, with the SLL being suppressed to a lower level, the antenna main beam will be broadened. For example, in Figure 6(a), by assuming a negligible back lobe level, the antenna beam efficiency has been improved from 12% to 97% by suppressing the SLL from –10 to –30 dB, but the 3-dB beamwidth has been increased from 12° to 16°. The beamwidths are also dependent on the number of elements in the array. With a 32 × 32-element array, the unsteered ($\phi_0 = 0^\circ$ and $\theta_0 = 0^\circ$) 3-dB beamwidth of the array factor is on the order of 3°, which is comparable with the 3-dB beamwidth of the reflector antenna used in the *SMAP* instrument. By using more elements, it is possible to achieve an even narrower beamwidth, down to 1 to 2° (dependent on the required SLLs) for a 64 × 64-element array, as shown in Figure 6(c).

PHASED ARRAY

Phased arrays have attracted great interest since the 1950s, and they have been used in a wide range of applications, such as radars, satellite communication, and imaging systems [36], [75]. The heart of a phased array lies in the analog phase shifters. The incoming signals of each antenna element in an antenna array are phase shifted and amplified/attenuated, and these signals are finally combined coherently by an analog combiner at the output. The general concept is shown in Figure 7.

The synthesized beam can be narrowed, widened, or steered to a particular angle using this technique. Analog phase shifters usually experience a tradeoff among phase resolution, phase error, amplitude error, and insertion loss (for passive phase shifters). Phase error and amplitude error introduce error in the synthesized beamwidth and steer angle. Phase resolution limits the steer angle resolution. However, this is not a problem since they can easily achieve 6 bits, even for discrete analog phase shifters, which is equivalent to 64 phase states and a phase resolution of 5.625° [76], [77]. Insertion loss is an extremely important factor, especially for radiometers, because this amplifies the system noise, according to [54]

$$N = (L-1)k_B TB, \tag{11}$$

where N is the noise added by the lossy component, L is the loss factor, k_B is the Boltzmann constant, T is the physical temperature of the component, and B is the bandwidth.

The added noise directly degrades the sensitivity of the radiometer by raising T_N in (1), (4), and (6), which can only be compensated for by increasing the system's bandwidth or integration time. Passive analog phase shifters have an insertion loss, typically ranging from 3 up to 14 dB at high frequencies (the L-band frequency and above) [78]–[83]. In [83], a low-cost p-i-n diode phase shifter, developed by the Monash Microwave, Antennas, RFID, and Sensors Laboratories (MMARS), has been designed and manufactured (Figure 8) for an L-band radiometer phased-array antenna. The insertion loss for this phase shifter for a combined 4 bits is 2 dB within a 25-MHz operating frequency, and the RMS phase error is less than 1° at 1.4 GHz and less than 3° within the operating bandwidth.

These performance parameters are excellent for developing a low-cost phased-array antenna for radiometric applications. The insertion loss in passive analog phase shifters can be avoided in active analog phase shifters, such as vector-sum phase shifters [76], [77], [84], with the expense of having greater power consumption of typically a few tens of milliwatts, depending on the design. Despite these drawbacks, a phased array offers a huge advantage in the system's computational and total power consumption over DBF.

L-BAND, APERTURE-COUPLED PATCH ANTENNA PHASED ARRAY

Two bits (180° and 90°) of the low-cost L-band p-i-n diode phase shifter shown in Figure 8 have been integrated into the design of a 4 × 4 L-band phased-array radiometer antenna as illustrated in Figure 9. This multilayer antenna is designed in an aperture-coupled microstrip patch structure, which allows the use of the low-cost FR-4 substrate in the radiating patch, creating sufficient room for

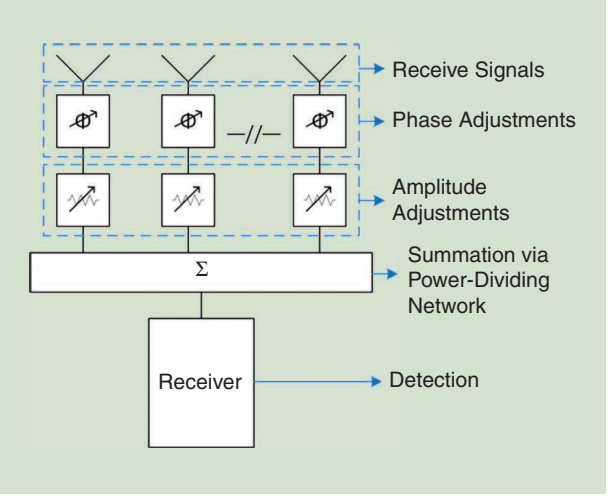

FIGURE 7. A concept for a phased array.

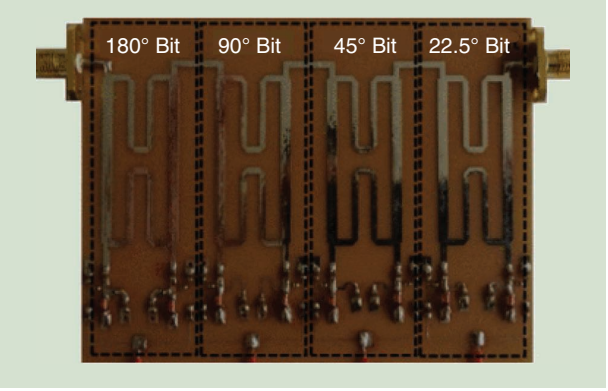

FIGURE 8. The L-band, low-cost p-i-n diode 4-bit phase shifter developed by MMARS. (Source: [83].)

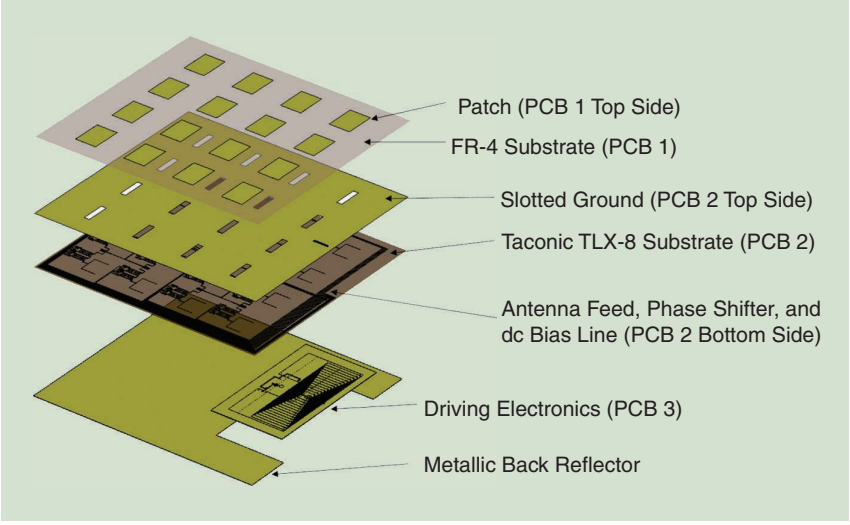

FIGURE 9. The overall layout of the L-band 4 × 4 phased array. PCB: printed circuit board.

the phase shifters and control network integration in the feedline layer.

Figure 10 shows the details of the antenna feedline layer design. In this design, a 1–16-way power divider with nonuniform amplitude distributions has been adopted to suppress the antenna SLL down to –25 dB. With the 2-bit phase shifters integrated into the feedline of each patch antenna and each phase shifter bit being independently controlled by dc bias lines, this phased array is capable of generating nine beams in 2D scanning. Those are ±20° beams in the x-direction, ±15° beams in the y-direction, and diagonal beams at angles (±19° x, ±17° y).

Figure 11 depicts the simulated radiation pattern results of the ±20° beam in the x-direction, and this antenna array exhibits a peak directivity of 18.5 dBi with a 3-dB beamwidth of 22°. The SLL is better than –27 dB on the H plane. The highest SLL on the electric field (E) plane is –25.2 dB at a 0° steered beam and –14.2 dB at ±20° steered beams.

The simulated diagonal beam at (–19° x, +17° y) is demonstrated in Figure 12. The corresponding phase assignment of each antenna element in the phased array is shown in Table 5, where the top left patch is assigned 0° of phase shift, and the bottom right patch is assigned 180° of phase shift. Overall, this simulation shows that this phased-array design can achieve a beam efficiency of >80% for all 1D steering beams and better than 77% for all diagonal beams at 1.4 GHz. The total loss is less than –1.85 dB for all beams at 1.4 GHz. This antenna design has been fabricated and is now under preparation for measurement.

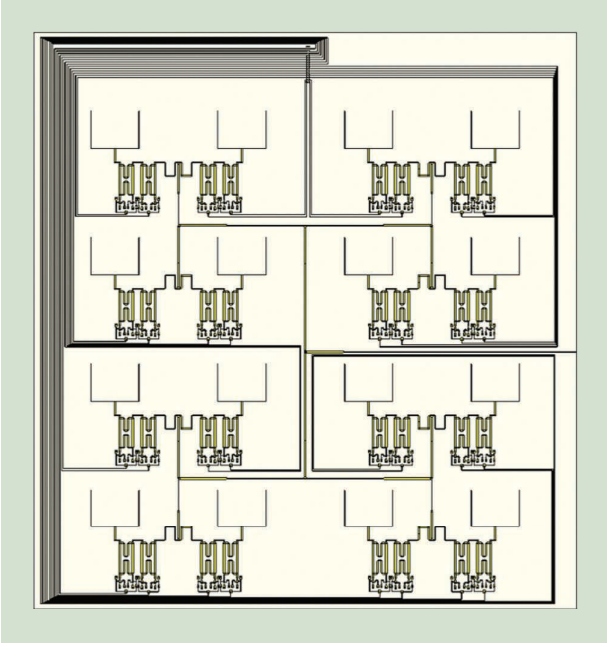

FIGURE 10. The feedline layer of a 4 × 4 L-band phased-array antenna.

DBF

Another way to achieve electronic beam forming is through performing the phase shift and amplitude tapering in the digital domain. Multiple antenna beams can be obtained simultaneously in the digital domain [36], [62], which allows smoother beam scanning as compared to that of a phased array [36].

The ability to accurately control multiple and simultaneous antenna beams directly benefits the push-broom scanning scheme, which is famous for its high sensitivity; more importantly, no moving parts are required for this scheme, which can significantly reduce the system's weight [85]. Additionally, the high sensitivity requirement is critical in ocean observations [85] whose parameters can also be measured by L-band radiometers like SMOS.

The main drawbacks of this scanning scheme are similar to those of a digital beam former and phased array operating in a multibeam configuration. They all need complex antenna systems and/or a large number of receivers [34], [85]. However, as technology progresses, it will be possible to develop cheap and lightweight receivers in the future [34]. Therefore, digital multibeam antennas in combination with a push-broom scanning scheme should be considered for compact and lightweight radiometers.

In DBF, the signal from each antenna element is sampled and multiplied by a corresponding complex weight, and these are then summed together to give the desired beam shape. Assuming input $X = [x_1, x_2, \ldots, x_M]^T, m = 1, \ldots, M$, where m is the mth antenna, a combining matrix W can be defined according to the following equations [36]:

$$W = \begin{bmatrix} W_1 \\ W_2 \\ \cdots \\ W_N \end{bmatrix} = \begin{bmatrix} W_{11} & \cdots & W_{1M} \\ \vdots & \ddots & \vdots \\ W_{N1} & \cdots & W_{NM} \end{bmatrix} \quad (12)$$

$$Y(\theta) = W_n^H X, \quad (13)$$

where $Y(\theta)$ is the output of the synthesized beam, and the H superscript indicates the Hermitian transpose. Different algorithms can be applied to generate a suitable set of weights to give a desired beam shape. Additionally, multibeam antennas can be realized with added complexity to only the digital processing unit [e.g., a field-programmable gate array (FPGA)] [36], [69], [86], which is more affordable compared to massive, lossy analog networks. Furthermore, amplitude and phase errors as in analog phase shifters no longer persist in digital phase shifters. However, the amplitudes and phases of the signals present at each channel (before the signals are digitized) must be approximately the same [63]; otherwise, errors will occur.

In multichannel radiometer systems [57], [62], [64], [69], compensations can be made by calibrating the system with a correlated noise signal. A common noise source will simultaneously inject its noise signal into each individual channel through a properly designed 1-to-N power divider, where N is the number of channels.

One channel is chosen as the reference channel, and then the signals of the other channels are sequentially cross correlated with the reference signal [62]. The obtained results are the compensation factors, which are used to correct the imbalances among channels. The gain differences among channels can also be corrected by using uncorrelated noise sources, which are usually temperature-controlled-matched loads at the input of each channel [62]. A typical example of DBF is depicted in Figure 13.

In [87], an 8–20-GHz receiver with selectable IFs for multibeam, phased-array DBF applications has been developed, using the SiGe BiCMOS technology. With some modifications, this module can be used to realize radiometer receivers with shared-aperture multiband antennas, which provides the benefits of high penetration at low frequency and improves the imaging resolution at high frequency.

The tradeoff for the excellent performance of DBF is the cost and power consumption of both the ADC and FPGA. Considering an 8 × 8-antenna array, the required number of ADCs is 64, and the processing speed of the FPGA should be

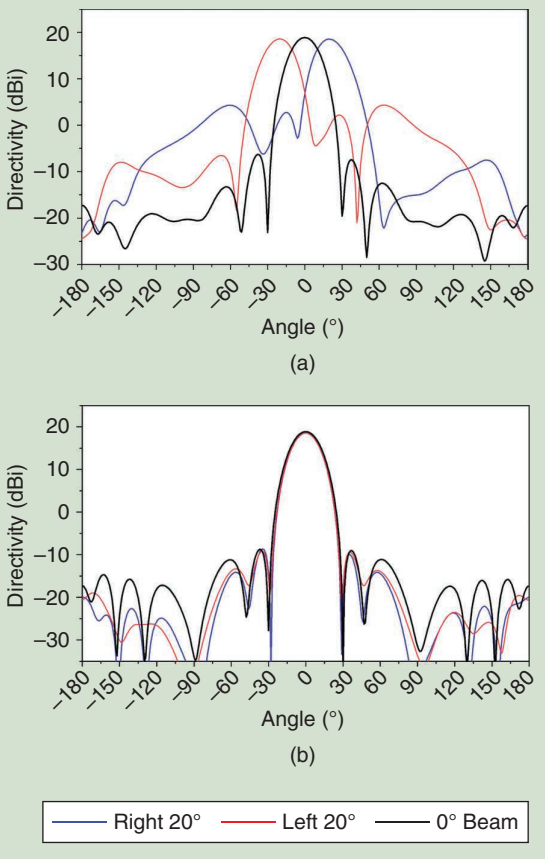

FIGURE 11. The simulation results of the radiation pattern of the 4 × 4 L-band phased-array antenna with its main beam steering at –20°, 0°, and 20° in the *x*-direction, showing the radiation pattern on the (a) E plane and (b) H plane.

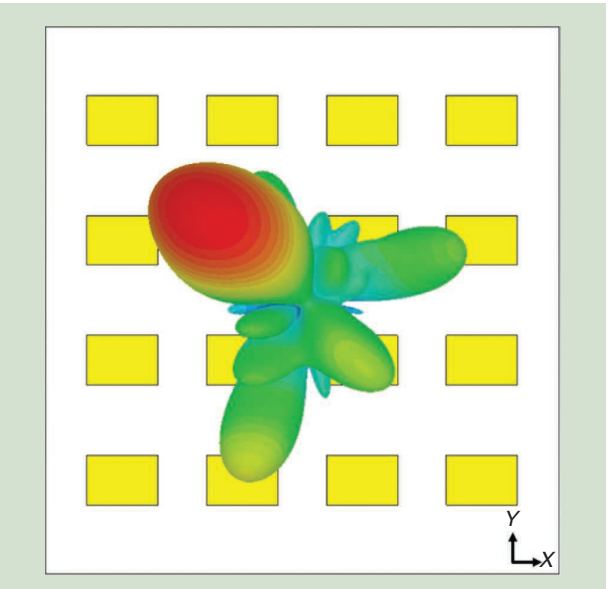

FIGURE 12. A simulated 3D radiation pattern of the 4 × 4 L-band phased-array antenna with the main beam steered at (–19° *x*, +17° *y*).

TABLE 5. THE PHASE ALLOCATION OF EACH ANTENNA ELEMENT TO GENERATE A (–19° *X*, +17° *Y*) BEAM.

0°	90°	180°	270°
90°	180°	270°	0°
180°	270°	0°	90°
270°	0°	90°	180°

at least 64 times faster than the sampling speed of one ADC unit. Multiple FPGAs can be used in parallel, but they have to be properly synchronized [88]. Again, the high cost of the DBF technique prevents it from being widely utilized in cost-effective systems as well as applications that use a massive number of antenna elements. Some techniques, such as using subarrays or hybrid beamforming techniques, have been devised to effectively reduce the number of channels required for a fixed number of antenna elements [36].

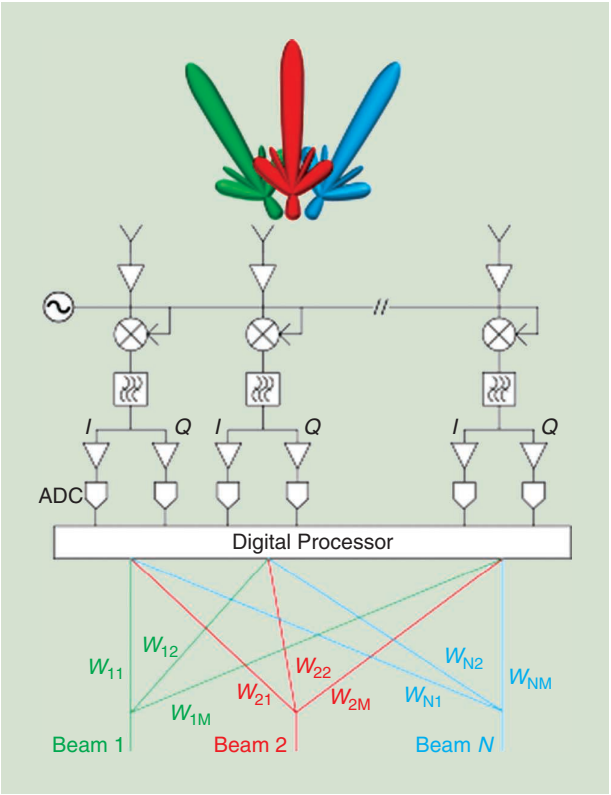

FIGURE 13. A DBF receiver. (Source: [36].)

SUBSTRATE-INTEGRATED WAVEGUIDE LONGITUDINAL SLOT-ARRAY ANTENNA

Another printable planar antenna structure that is also suitable for microwave radiometers is the substrate-integrated waveguide (SIW) slot antenna. The waveguide slot antenna demonstrates excellent performance in phased-array designs because of its low loss at microwave frequencies, high quality factor, and high-power-handling capability. Due to the space limitations of the airborne radiometer systems, the SIW, which is a planar form of the conventional waveguide, exhibits promising aspects.

The first SIW technology was introduced through a patent in 1994 [89], with a complete antenna array system developed in 1998 [90]. A regular SIW structure is formed by placing several conducting via holes to form the E-field shield, and, thus, the structure is completely compatible with the conventional multilayer microwave integrated circuits fabrication process, such as low-temperature cofired ceramics or multilayer printed board circuits (PCB) [91]. A high-gain SIW 8 × 8 longitudinal slot array antenna at the Ku band was developed by the MMARS laboratory, as shown in Figure 14(a). The proposed antenna had a return-loss bandwidth of 500 MHz (18.5–18.9 GHz) and maximum gain of 21 dB, with a 3-dB beamwidth of 13.5°. Thus, it exhibits the maximum merits of the conventional

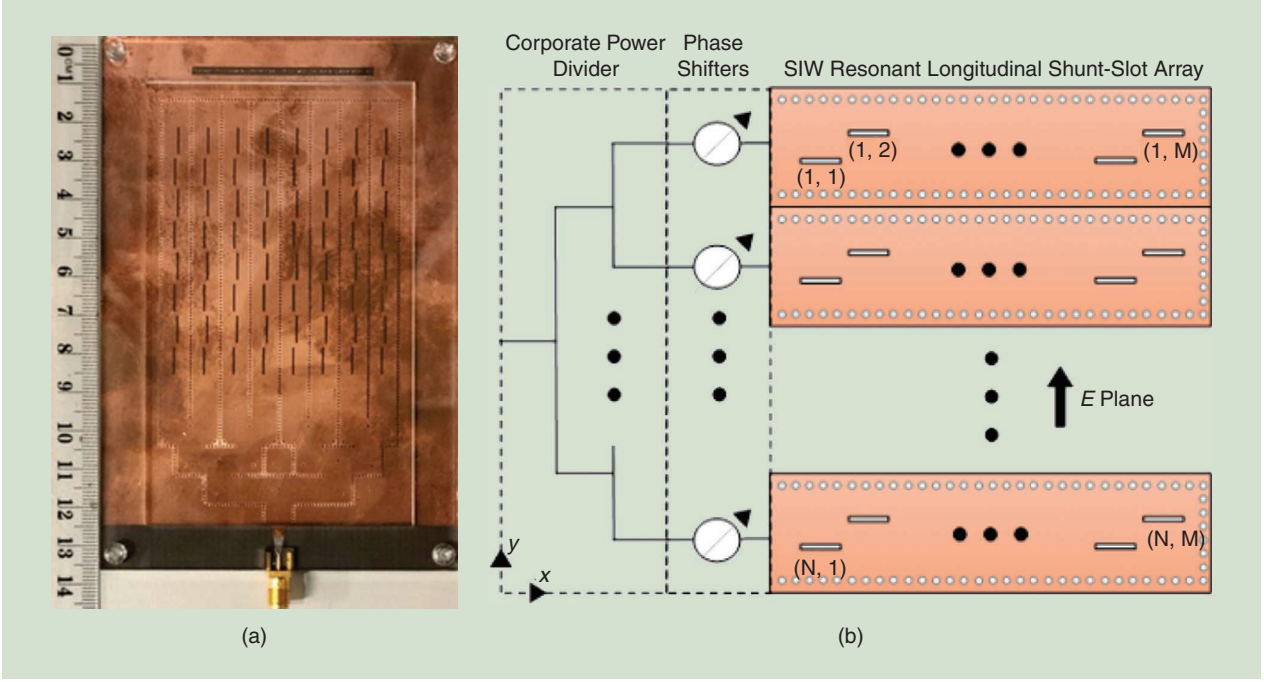

FIGURE 14. The SIW slotted-array configurations: (a) an 8 × 8 SIW longitudinal slot-array antenna and (b) a phased-array slotted waveguide topology.

waveguide structures, along with a low-cost fabrication capability and planar structure similar to the patch antennas.

The SIW slotted-array antennas can be compared with the stick array, where the number of linear stick arrays can be excited by a power divider through phase shifters to form a phased-array system, as shown in Figure 14(b). Depending on the application requirements and the selection of the number of phase shifter bits, the beamforming can be achieved in one plane, i.e., the E plane, as shown in Figure 15.

PATCH ANTENNA AND SIW PHASED ARRAY FOR REPLACING HORN ANTENNAS IN AIRBORNE AND SPACEBORNE PLATFORMS

Due to the nonconformal structure and long body length, it is difficult to install and mount conventionally used horn antennas into aircraft without significant modifications. In certain cases, a bulky antenna structure could also affect the aerodynamics of the airplane [92].

In contrast, both a microstrip patch phased array and an SIW array can be implemented in low profile and planar forms, leading to easy deployments. For example, both the EMIRAD and Cooperative Airborne Radiometer for Ocean and Land Studies (CAROLS) adopted two large Potter horns, each with a total length of more than 150 cm (including the orthomode transducer) [93]–[95]. The antenna body, excluding the orthomode transducer, is shown in Figure 16(b). These, in turn, require modifications to the aircraft, especially precise designs of the interface between the horn antennas and aircraft [as shown in Figure 16(c) and (d)]; further antenna details and the interface design are available in [95].

In contrast, the Polarimetric L-band Multibeam Radiometer (PLMR) antenna has a height of only 20 cm [including the receiver and radome, as shown in Figure 16(a)] [96], leading to a relatively easy installation on small airplanes. Furthermore, compared to an aperture-coupled patch antenna (ACPA) phased array (as discussed in the "L-Band Aperture-Coupled Patch Antenna Phased Array" section), SIW arrays have the merit of implementation in a single layer, while ACPA arrays require multilayer structures. However, this single-layer design has the capability of scanning in only 1D. To realize 2D scanning similar to the patch antenna arrays, multiple layers with much higher complexity are required for an SIW (examples in [97]–[99]).

In addition to being strong candidates for replacing horn antennas in airborne platforms, the mentioned antenna structures also have the potential to be deployed in spaceborne platforms as an alternative approach to feed a large reflector antenna. As discussed in [100], to achieve less than a 1.5°, 3-dB beamwidth—hence, a less-than-20-km footprint from LEO—using patch arrays could reduce the weight by a factor of three and the length by a factor of six, with a similar performance to that of a conventional horn illuminating a 12-m reflector.

For future high-resolution L-band radiometric soil moisture mapping with a spatial resolution of better than 10 km, a system with multiple feeds and an antenna aperture of more than 25 m may be required [101], [102]. Even though the required reflector size may be large to achieve the desired <10-km spatial resolution, deployable mesh reflectors, such as those used in *SMAP*, can be employed to minimize the prelaunch system's size and weight. By using multiple small patch or SIW arrays (e.g., 3×3 or 4×4 each) in a hexagonal configuration (to increase the swath width [102]) for a light weight and profile, the authors envision that the mechanical rotating part of the reflector could be replaced by the discussed electronic beam-steering techniques.

DISCUSSION AND CONCLUSION

This article reviewed microwave radiometers for remotely measuring the moisture content within soils and explored methods to realize a lightweight, compact, and cost-saving radiometer. The antenna system plays a vital role in the radiometer system, but it is a challenging task to design in a compact and lightweight manner, with a narrow beamwidth at low-operating-frequency bands, such as the L band [33], [53], [67]. The aperture-synthesis technique can be used to eliminate the dependency of a radiometer's spatial resolution on the antenna's real-aperture dimension, but the system sensitivity is reduced as a consequence [17], [34], [67].

The *SMAP* instrument uses a mechanical system to steer the antenna main beam conically (i.e., with a fixed incident

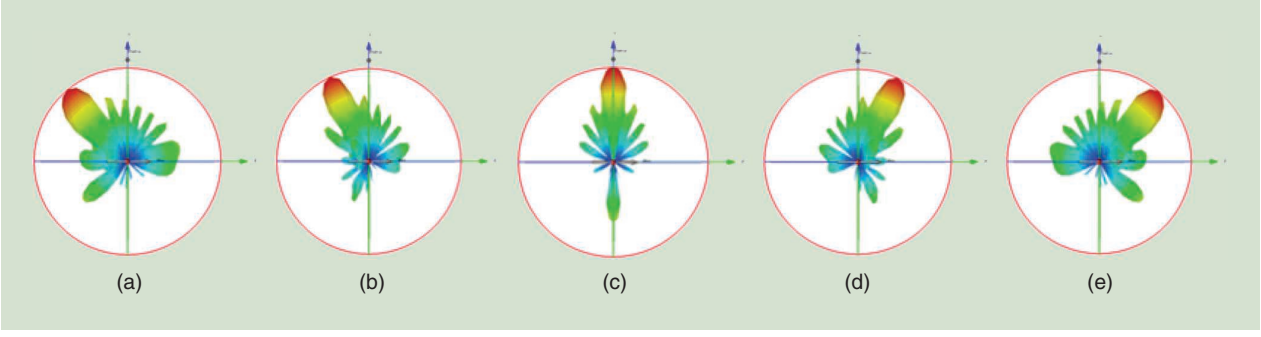

FIGURE 15. A 3D radiation pattern of the SIW slotted-array antenna with different phase angles: (a) –120°, (b) –80°, (c) 0°, (d) 80°, and (e) 120°.

angle), while the *SMOS* radiometer (MIRAS) uses the synthetic aperture technique to obtain multiangular measurements. The *SMAP* instrument's radiometer achieves better sensitivity, but it has to employ a large antenna aperture and heavy spin subsystem. Conversely, the synthetic aperture technique allows MIRAS to employ an array of smaller antennas, but its radiometer sensitivity is reduced.

Electronic beamforming techniques, which have been investigated by several researchers [60], [62], [69], can also be utilized to simultaneously achieve excellent antenna beam shapes as well as dynamically create agile beams for different viewing angles, with minimal sacrifice to the system's sensitivity.

Analog beamforming techniques or, specifically, phased arrays require less hardware complexity but lack the flexibility in beam scanning and SLL reconfiguration that the DBF technique could provide. Conversely, digital beam formers' reliance on a large number of ADCs and high-speed digital processing units can make them expensive in terms of both cost and power consumption. Nevertheless, with the use of digital radiometers and DBF techniques, benefits such as accuracy, stability, reconfigurability, and multibeam scanning ability can be obtained from the digital signal processing algorithms.

Along with the development of electronic circuits in the future, when integrated circuits are of low loss at microwave frequency bands, such as the L band, and digital circuits are cheaper, faster, and smaller, digital radiometers using DBF techniques for fast scanning can create a significant impact on the next generation of soil moisture remote sensing radiometers. Additionally, by exploiting the ability to smoothly control the multibeam antennas of digital beam formers, the push-broom scanning scheme can also be utilized to achieve highly sensitive yet compact radiometer systems.

Printable planar antenna structures, such as patch and SIW, are viable options for low-cost, compact, and lightweight radiometers [101], [103]. The MMARS Laboratory

(a)

(b)

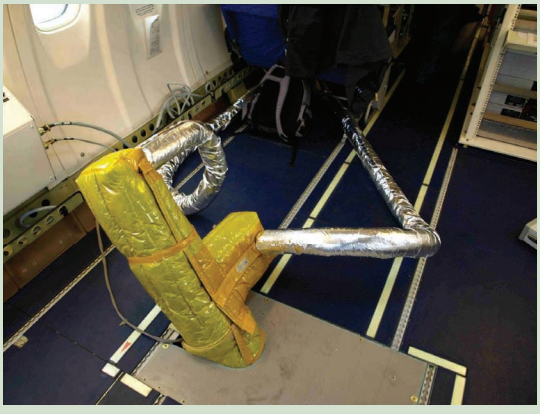

(c)

(d)

FIGURE 16. (a) A PLMR planar structure. (Source: [104].) (b) A Potter horn antenna used in the CAROLS and EMIRAD radiometers. (Source: [93].) (c) A CAROLS horn antenna installed on an aircraft. (Source: [18].) (d) EMIRAD horn antennas installed on an aircraft. (Source: [93]).

has developed an L-band, aperture-coupled patch antenna phased array and a Ku-band, SIW longitudinal slot-array antenna suitable for airborne dual-band (L- and Ku-band) radiometer systems and also for the demonstration of design concepts for a future spaceborne system.

It is also expected that more research activities will focus on low-loss, printable planar antennas/antenna arrays with electronic beam-steering capability to miniaturize next-generation radiometer systems. In other words, in the future, it will be possible to realize a compact, lightweight, economical, yet accurate radiometer system with the use of a low-loss, printable planar antenna array in combination with digital radiometers and electronic beamformers.

ACKNOWLEDGMENT

The authors would like to thank Dr. Lilian Khaw for her proofreading and writing suggestions. The authors would also like to thank all of the authors of the referred publications for giving permissions/high-resolution images to be reused in this paper. This work was supported by the Australian Research Council through "Passive Airborne Radiometer for Soil Moisture Monitoring" under grant DP160104233. Trong Khoa Ho and Jiewei Feng are cofirst authors. Trong Khoa Ho is the corresponding author.

AUTHOR INFORMATION

Trong Khoa Ho (trong.ho@monash.edu) is with the Department of Electrical and Computer Systems Engineering, Monash University, Clayton, Victoria, 3800, Australia.

Jiewei Feng (jiewei.feng1@monash.edu) is with the Department of Electrical and Computer Systems Engineering, Monash University, Clayton, Victoria, 3800, Australia.

Farah Bilawal (farah.bilawal@monash.edu) is with the Department of Electrical and Computer Systems Engineering, Monash University, Clayton, Victoria, 3800, Australia.

Shahriar Hasan Shehab (shahriar.shehab@monash.edu) is with the Department of Electrical and Computer Systems, Monash University, Clayton, Victoria, 3800, Australia.

Kim Tuyen Trinh (kim.trinh@monash.edu) is with the Department of Electrical and Computer Systems Engineering, Monash University, Clayton, Victoria, 3800, Australia.

Yang Yang (yang.yang-1@uts.edu.au) is with the School of Electrical and Data Engineering, University of Technology Sydney, Ultimo, New South Wales, 2007, Australia.

Christoph Rüdiger (chris.rudiger@monash.edu) is with the Department of Civil Engineering, Monash University, Clayton, Victoria, 3800, Australia.

Jeffrey P. Walker (jeff.walker@monash.edu) is with the Department of Civil Engineering, Monash University, Clayton, Victoria, 3800, Australia.

Nemai Chandra Karmakar (nemai.karmakar@monash.edu) is with the Department of Electrical and Computer Systems Engineering, Monash University, Clayton, Victoria, 3800, Australia.

REFERENCES

[1] A. C. M. Beljaars, P. Viterbo, M. J. Miller, and A. K. Betts, "The anomalous rainfall over the United States during July 1993: Sensitivity to land surface parameterization and soil moisture anomalies," *Mon. Weather Rev.*, vol. 124, no. 3, pp. 362–383, 1996. doi: 10.1175/1520-0493(1996)124<0362:TAROTU>2.0.CO;2.

[2] "Mission to planet earth strategic enterprise plan 1996–2002," Nat. Aeronautics Space Admin., NASA, Washington, D. C., 1996.

[3] J. Walker et al., "High resolution soil moisture mapping," in *Proc. 5th Global Workshop on Digital Soil Mapping Digital Soil Assessments Beyond*, 2012. doi: 10.1201/b12728-11.

[4] Y. H. Kerr and Y. H. Kerr, "Soil moisture from space: Where are we?" *Hydrogeol. J.*, vol. 15, no. 1, pp. 117–120, 2007. Doi: 10.1007/s10040-006-0095-3.

[5] M. S. Yee, J. Walker, C. Rüdiger, R. Parinussa, T. Koike, and Y. Kerr, "A comparison of SMOS and AMSR2 soil moisture using representative sites of the OzNet monitoring network," *Remote Sens. Environ.*, vol. 195, pp. 297–312, June 2017. doi: 10.1016/j.rse.2017.04.019.

[6] O. P. N. Calla and B. Deka, "Study of emissivity of dry and wet loamy sand soil at microwave frequency," *Indian J. Radio Space Phys.*, vol. 29, pp. 140–145, June 2000.

[7] O. P. N. Calla, R. Vyas, D. Bohra, and A. Arora, "Hstudy of emission behavior of dry and wet soil at microwave frequency," Presented at Int. conf. Commun. Electron. (ICECC-08), University of Rajashahi, Bangladesh.

[8] D. Entekhabi et al., "The soil moisture active/passive mission (SMAP)," in *Proc. IEEE Int. Geoscience Remote Sensing Symp. (IGARSS 2008)*, July 2008, vol. 3. doi: 10.1109/IGARSS.2008.4779267.

[9] E. R. Westwater, "The accuracy of water vapor and cloud liquid determination by dual frequency ground-based microwave radiometry," *Radio Sci.*, vol. 3, no. 4, pp. 677–685, July 1978. doi: 10.1029/RS013i004p00677.

[10] H. M. J. Barre, B. Duesmann, and Y. H. Kerr, "SMOS: The mission and the system," *IEEE Trans. Geosci. Remote Sens.*, vol. 46, no. 3, pp. 587–593, Mar. 2008. doi: 10.1109/TGRS.2008.916264.

[11] B. Aja et al., "Very low-noise differential radiometer at 30 GHz for the PLANCK LFI," *IEEE Trans. Microw. Theory Techn.*, vol. 53, no. 6, pp. 2050–2062, June 2005. doi: 10.1109/TMTT.2005.848815.

[12] O. P. N. Calla et al., "Measurement of soil moisture using microwave radiometer," in *Proc. Int. Conf. Recent Adv. Microw. Theory Appl.*, Nov. 2008.

[13] D. Entekhabi, E. G. Njoku, P. E. O'Neill, K. Kellogg, and J. Entin, "The NASA soil moisture active passive (SMAP) mission formulation," in *Proc. IEEE Int. Geosci. Remote Sens. Symp.*, July 2011. doi: 10.1109/IGARSS.2011.6049669.

[14] F. T. Ulaby, R. K. Moore, and A. K. Fung, *Microwave Remote Sensing: Active and Passive*. Reading, MA: Addison-Wesley, 1981.

[15] W. Wagner et al., "Operational readiness of microwave remote sensing of soil moisture for hydrologic applications," *Hydrol. Res.*, vol. 38, no. 1, pp. 1–20, 2007. doi: 10.2166/nh.2007.029.

[16] K. Kornelsen and P. Coulibaly, "Advances in soil moisture retrieval from synthetic aperture radar and hydrological applications," *J. Hydrol.*, vol. 476, pp. 460–489, Jan. 2013. doi: 10.1016/j.jhydrol.2012.10.044.

[17] Y. H. Kerr et al., "The SMOS mission: New tool for monitoring key elements of the global water cycle," *Proc. IEEE*, vol. 98, no. 5, pp. 666–687, May 2010. doi: 10.1109/JPROC.2010.2043032.

[18] M. Pardé et al.," "Radio frequency interferences investigation using the airborne L-band full polarimetric radiometer CAROLS," in *Proc. 2010 11th Specialist Meeting Microwave Radiometry Remote Sens. Environ.*, Washington, D. C., pp. 300–305. doi: 10.1109/MICRORAD.2010.5559530.

[19] N. J. Rodríguez-Fernández et al., "SMOS-HR: A high resolution l-band passive radiometer for earth science and applications," in *Proc. 2019 IEEE Int. Geoscience Remote Sensing Symp. (IGARSS 2019)*, Yokohama, Japan, pp. 8392–8395. doi: 10.1109/IGARSS.2019.8897815.

[20] N. Reul et al., "Sea surface salinity estimates from spaceborne L-band radiometers: An overview of the first decade of observation (2010– 2019)," *Remote Sens. Environ.*, vol. 242, June 2020. Art. no. 111769. doi: 10.1016/j.rse.2020.111769.

[21] G. Lagerloef et al., "The Aquarius/Sac-D mission: Designed to meet the salinity remote-sensing challenge," *Oceanography*, vol. 21, no. 1, pp. 68–81, 2008. doi: 10.5670/oceanog.2008.68.

[22] K. Rautiainen, J. Lemmetyinen, J. Ikonen and J. Pulliainen, "Algorithm theoretical baseline document," National Skill Development Corporation, Feb. 28, 2019. Accessed: Feb. 2021. [Online]. Available: https://nsdc.fmi.fi/services/SMOSService/docs/FTS-ATBD.pdf

[23] "SMOS Level 3 Soil freeze/Thaw service," Finnish Meteorological Institute, European Space Agency, Madrid, Spain. Accessed: Feb. 2021. [Online]. Available: https://nsdc.fmi.fi/services/SMOSService/

[24] "Aquarius L3 weekly polar-gridded landscape freeze/thaw data, Version 5," National Snow and Ice Data Center. Accessed: Feb. 2021. [Online]. Available: https://nsidc.org/data/AQ3_FT/versions/5. [Accessed Feb 2021].

[25] "SMAP Data," National Snow and Ice Data Center. Accessed: Feb. 2021. [Online]. Available: https://nsidc.org/data/smap/smap-data.html

[26] "SMAP wind speeds remote sensing systems," Remote Sensing Systems, Feb. 5, 2018. Accessed: Feb. 2021. [Online]. Available: http://www.remss.com/missions/smap/winds/

[27] N. Reul, J. Tenerelli, B. Chapron, D. Vandemark, Y. Quilfen, and Y. Kerr, "SMOS satellite L-band radiometer: A new capability for ocean surface remote sensing in hurricanes," *J. Geophys. Res.–Oceans*, vol. 117, no. C2, pp. C02006-1–C02006-24, Feb. 2012. doi: 10.1029/2011JC007474.

[28] "SMOS wind data service and storm projects," Ifremer. Accessed: Feb. 2021. [Online]. Available: https://www.smosstorm.org/

[29] S. Mecklenburg et al., "ESA's Soil Moisture and Ocean Salinity mission: From science to operational applications," *Remote Sens. Environ*, vol. 180, pp. 3–18, July 2016. doi: 10.1016/j.rse.2015.12.025.

[30] R. Ricker and T.-K. Xiangshan, "SMOS sea ice thickness," Alfred Wegener Institute, 27 Mar 2020. Accessed: Feb. 2021. [Online]. Available: https://spaces.awi.de/display/CS2SMOS/SMOS+Sea+Ice+Thickness

[31] E. Zapata, "The state of play US space systems competitiveness: Prices, productivity, and other measures of launchers & spacecraft," NASA Kennedy Space Center, Oct. 11, 2017. Accessed: July 19, 2020. [Online]. Available: https://ntrs.nasa.gov/archive/nasa/casi.ntrs.nasa.gov/20170012517.pdf

[32] D. Entekhabi et al., "The soil moisture active passive (SMAP) mission," *Proc. IEEE*, vol. 98, no. 5, pp. 704–716, May 2010. doi: 10.1109/JPROC.2010.2043918.

[33] Y. Kerr et al., "New radiometers: SMOS-a dual pol L-band 2D aperture synthesis radiometer," in *Proc. 2000 IEEE Aerospace Conf. (Cat. No.00TH8484)*, Big Sky, MT, vol. 5, pp. 119–128. doi: 10.1109/AERO.2000.878481.

[34] N. Skou and M. Le Vine, *Microwave Radiometer Systems: Design and Analysis.* Boston: Artech House, 2006.

[35] D. M. Le Vine, C. T. Swift, and M. Haken, "Development of the synthetic aperture microwave radiometer, ESTAR," *IEEE Trans. Geosci. Remote Sens.*, vol. 39, no. 1, pp. 199–202, Jan. 2001. doi: 10.1109/36.898685.

[36] W. Hong et al, "Multibeam antenna technologies for 5G wireless communications," in *IEEE Trans. Antennas Propag.*, vol. 65, no. 12, pp. 6231–6249, Dec. 2017. doi: 10.1109/TAP.2017.2712819.

[37] K. Kellogg et al.," "NASA's soil moisture active passive (SMAP) observatory," in *Proc. 2013 IEEE Aerospace Conf.*, Big Sky, MT, 2013, pp. 1–20. doi: 10.1109/AERO.2013.6496938.

[38] D Entekhabi, E Njoku, P O'Neill, "The soil moisture active and passive mission (SMAP): Science and applications," in *Proc. 2009 IEEE Radar Conf.*, Pasadena, CA, May 4–8, 2009, Paper 3172.

[39] C. Derksen et al., "Retrieving landscape freeze/thaw state from Soil Moisture Active Passive (SMAP) radar and radiometer measurements," *Remote Sens. Environ.*, vol. 194, pp. 48–62, June 2017. doi: 10.1016/j.rse.2017.03.007.

[40] "SMAP Enhanced L3 Radiometer Global and Northern Hemisphere Daily 9 km EASE-Grid Freeze/Thaw State, Version 3," National Snow and Ice Data Center. Accessed: Feb. 2021. [Online]. Available: https://nsidc.org/data/SPL3FTP_E/versions/3

[41] S. Mecklenburg et al., "ESA's soil moisture and ocean salinity mission: from science to operational applications," *Remote Sens. Environ.*, vol. 180, pp. 3–18, July 2016. doi: 10.1016/j.rse.2015.12.025.

[42] D. M. L. Vine, "The sensitivity of synthetic aperture radiometers for remote sensing applications from space," *Radio Sci.*, vol. 25, no. 04, pp. 441–453, July–Aug. 1990. doi: 10.1029/RS025i004p00441.

[43] "SMOS - eoPortal Directory - Satellite missions," eoPortal Directory, 2020. Accessed: May 4, 2020. [Online]. Available: https://directory.eoportal.org/web/eoportal/satellite-missions/s/smos

[44] "SMAP - eoPortal Directory - Satellite missions," eoPortal Directory, 2020. Accessed: May 4, 2020. [Online]. Available: https://directory.eoportal.org/web/eoportal/satellite-missions/s/smap

[45] J. R. Piepmeier et al., "Radio-frequency interference mitigation for the soil moisture active passive microwave radiometer," *IEEE Trans. Geosci. Remote Sens.*, vol. 52, no. 1, pp. 761–775, Jan. 2014. doi: 10.1109/TGRS.2013.2281266.

[46] E. Daganzo-Eusebio, R. Oliva, Y. H. Kerr, S. Nieto, P. Richaume, and S. M. Mecklenburg, "SMOS radiometer in the 1400–1427-MHz passive band: Impact of the RFI environment and approach to its mitigation and cancellation," *IEEE Trans. Geosci.*

Remote Sens., vol. 51, no. 10, pp. 4999–5007, Oct. 2013. doi: 10.1109/TGRS.2013.2259179.

[47] E. Uranga, A. Llorente, A. de la Fuente, E. Daganzo, R. Oliva and Y. Kerr, "Radio frequency interference devices: The SMOS experience," in *Proc. 2019 IEEE Int. Geoscience Remote Sens. Symp. (IGARSS 2019)*, Yokohama, Japan, pp. 4528–4531. doi: 10.1109/IGARSS.2019.8900261.

[48] E. Uranga, Á. Llorente and A. d. la Fuente, "DATABASE OF SMOS RFI SOURCES IN THE 1400-1427MHZ PASSIVE BAND," in *Proc. 2018 IEEE Global Conf. Signal Inform. Process. (GlobalSIP)*, Anaheim, CA, pp. 1095–1098. doi: 10.1109/GlobalSIP.2018.8646378.

[49] M. Spencer, S. Chan, E. Belz, J. Piepmeier, P. Mohammed, and E. Kim, "Radio frequency interference mitigation for the planned SMAP radar and radiometer," in *Proc. Int. Geoscience Remote Sens. Symp. (IGARSS)*, Vancouver, Canada, July 24–29, 2011.

[50] S. K. Chan et al., "Assessment of the SMAP passive soil moisture product," *IEEE Trans. Geosci. Remote Sens.*, vol. 54, no. 8, pp. 4994–5007, Aug. 2016. doi: 10.1109/TGRS.2016.2561938.

[51] J. R. Piepmeier et al., "SMAP L-band microwave radiometer: instrument design and first year on orbit," *IEEE Trans. Geosci. Remote Sens.*, vol. 55, no. 4, pp. 1954–1966, Apr. 2017. doi: 10.1109/TGRS.2016.2631978.

[52] K. D. McMullan et al., "SMOS: The payload," *IEEE Trans. Geosci. Remote Sens.*, vol. 46, no. 3, pp. 594–605, Mar. 2008. doi: 10.1109/TGRS.2007.914809.

[53] A. Colliander, F. Torres, and I. Corbella, "Correlation denormalization in interferometric or polarimetric radiometers: A unified approach," *IEEE Trans. Geosci. Remote Sens.*, vol. 47, no. 2, pp. 561–568, Feb. 2009. doi: 10.1109/TGRS.2008.2003247.

[54] D. Pozar, *Microwave Engineering*. Hoboken, NJ: Wiley, 2005.

[55] R. H. Dicke, "The measurement of thermal radiation at microwave frequencies," *Rev. Sci. Instr.*, vol. 17, no. 7, pp. 268–279, 1946. doi: 10.1063/1.1770483.

[56] I. Corbella et al., "MIRAS end-to-end calibration: Application to SMOS L1 processor," *IEEE Trans. Geosci. Remote Sens.*, vol. 43, no. 5, pp. 1126–1134, May 2005. doi: 10.1109/TGRS.2004.840458.

[57] A. Colliander et al., "MIRAS reference radiometer: A fully polarimetric noise injection radiometer," *IEEE Trans. Geosci. Remote Sens.*, vol. 43, no. 5, pp. 1135–1143, 2005. doi: 10.1109/tgrs.2004.840667.

[58] L. Tsang, J. A. Kong, and R. T. Shin, *Theory of Microwave Remote Sensing*. New York: Wiley, 1999.

[59] J. Ohlson and J. Swett, "Digital radiometer performance," *IEEE Trans. Aerosp. Electron. Syst.*, vol. AES-9, no. 6, pp. 864–874, 1973. doi: 10.1109/taes.1973.309661.

[60] A. Camps, X. Bosch-Lluis, I. Ramos-Perez, J. Marchan-Hernandez, B. Izquierdo, and N. Rodriguez-Alvarez, "New instrument concepts for ocean sensing: Analysis of the PAU-radiometer," *IEEE Trans. Geosci. Remote Sens.*, vol. 45, no. 10, pp. 3180–3192, 2007. doi: 10.1109/tgrs.2007.894925.

[61] X. Bosch-Lluis et al., "The impact of the number of bits in digital beamforming real aperture and synthetic aperture radiometers," in *Proc. Microw. Radiometry Remote Sens. Environ.*, Firenze, 2008, pp. 1–4.

[62] X. Bosch-Lluis, I. Ramos-Perez, A. Camps, N. Rodriguez-Alvarez, E. Valencia, and J. Marchan-Hernandez, "Description and performance of an L-band radiometer with digital beamforming," *Remote Sens.*, vol. 3, no. 1, pp. 14–40, 2010. doi: 10.3390/rs3010014.

[63] X. Bosch-Lluis, A. Camps, I. Ramos-Perez, J. Marchan-Hernandez, N. Rodriguez-Alvarez, and E. Valencia, "PAU/RAD: Design and preliminary calibration results of a new L-band pseudo-correlation radiometer concept," *Sensors*, vol. 8, no. 7, pp. 4392–4412, 2008. doi: 10.3390/s8074392.

[64] J. Rotbøll, S. Søbjaerg, and N. Skou, "A novel L-band polarimetric radiometer featuring subharmonic sampling," *Radio Sci.*, vol. 38, no. 3, 2003. doi: 10.1029/2002rs002666.

[65] M. Fischman and A. England, "Sensitivity of a 1.4 GHz direct-sampling digital radiometer," *IEEE Trans. Geosci. Remote Sens.*, vol. 37, no. 5, pp. 2172–2180, 1999. doi: 10.1109/36.789614.

[66] D. M. Le Vine, A. J. Griffis, C. T. Swift, and T. J. Jackson, "ESTAR: A synthetic aperture microwave radiometer for remote sensing applications," *Proc. IEEE*, vol. 82, no. 12, pp. 1787–1801, Dec. 1994. doi: 10.1109/5.338071.

[67] D. Le Vine, "Synthetic aperture radiometer systems," *IEEE Trans. Microw. Theory Techn.*, vol. 47, no. 12, pp. 2228–2236, 1999. doi: 10.1109/22.808964.

[68] E. G. Njoku, "Passive microwave remote sensing of the earth from space: A review," *Proc. IEEE*, vol. 70, no. 7, pp. 728–750, July 1982. doi: 10.1109/PROC.1982.12380.

[69] Z. Jing, L. Qingxia, and G. Wei, "A multichannel passive imaging radiometer using DBF technique," *IEEE Geosci. Remote Sens. Lett.*, vol. 7, no. 2, pp. 329–332, 2010. doi: 10.1109/lgrs.2009.2034671.

[70] H. J. Kramer, "SMAP (Soil Moisture Active/Passive) mission," ESA. Accessed: Feb. 2021. [Online]. Available: https://earth.esa.int/web/eoportal/satellite-missions/s/smap

[71] M. Hassan and N. Karmakar, "Comparative study of different power distribution methods for array antenna beamforming for soil moisture radiometer," in *Proc. 2017 11th Int. Conf. Sensing Technol. (ICST)*, Sydney, NSW, pp. 1–4. doi: 10.1109/ICSensT.2017.8304480.

[72] W. Li, X. Huang, and H. Leung, "Performance evaluation of digital beamforming strategies for satellite communications," *IEEE Trans. Aerosp. Electron. Syst.*, vol. 40, no. 1, pp. 12–26, 2004. doi: 10.1109/taes.2004.1292139.

[73] A. Safaai-Jazi, "A new formulation for the design of Chebyshev arrays," *IEEE Trans. Antennas Propag.*, vol. 42, no. 3, pp. 439–443, 1994. doi: 10.1109/8.280736.

[74] C. A. Balanis, *Antenna Theory: Analysis and Design*. Hoboken, NJ: Wiley, 2016.

[75] D. Liu, B. Gaucher, U. Pfeiffer, and J. Grzyb, "Advanced millimeter-wave technologies," *Phys. Rev.*, vol. 134, pp. A635–A646, Dec. 1965.

[76] B. Cetindogan, E. Ozeren, B. Ustundag, M. Kaynak, and Y. Gurbuz, "A 6 bit vector-sum phase shifter with a decoder based control circuit for X-band phased-arrays," *IEEE Microw. Compon. Lett.*, vol. 26, no. 1, pp. 64–66, 2016. doi: 10.1109/lmwc.2015.2505618.

[77] M. Mohsenpour and C. Saavedra, "Variable 360° vector-sum phase shifter with coarse and fine vector scaling," *IEEE Trans.*

Microw. Theory Techn., vol. 64, no. 7, pp. 2113–2120, 2016. doi: 10.1109/tmtt.2016.2574843.

[78] T. Lambard, O. Lafond, M. Himdi, H. Jeuland, and S. Bolioli, "A novel analog 360° phase shifter design in Ku and Ka bands," *Microwave Opt. Technol. Lett.*, vol. 52, no. 8, pp. 1733–1736, 2010. doi: 10.1002/mop.25307.

[79] T. Li and H. Wang, "A millimeter-wave fully integrated passive reflection-type phase shifter with transformer-based multi-resonance loads for 360° phase shifting," *IEEE Trans. Circuits Syst. I, Reg. Papers*, vol. 65, no. 4, pp. 1406–1419, 2018. doi: 10.1109/tcsi.2017.2748078.

[80] Y. Tousi and A. Valdes-Garcia, "A Ka-band digitally-controlled phase shifter with sub-degree phase precision," in *Proc. IEEE Radio Frequency Integrated Circuits Symp.*, May 2016, pp. 356–359. doi: 10.1109/RFIC.2016.7508326.

[81] W. H. Woods, A. Valdes-Garcia, H. Ding, and J. Rascoe, "CMOS millimeter wave phase shifter based on tunable transmission lines," in *Proc. IEEE Custom Integr. Circuits Conf.*, Sept. 2013, pp. 1–4. doi: 10.1109/CICC.2013.6658442.

[82] J. Zhang and D. Zhao," "A Ka-band 360° digitally-controlled passive phase shifter in 65-nm CMOS," in *Proc. 2018 IEEE Int. Symp. Radio-Frequency Integration Technol. (RFIT)*, Melbourne, VIC, pp. 1–3. doi: 10.1109/RFIT.2018.8524072.

[83] K. T. Trinh, J. Feng, S. H. Shehab, and N. C. Karmakar, "1.4 GHz low-cost PIN diode phase shifter for L-band radiometer antenna," *IEEE Access*, vol. 7, pp. 95,274–95,284, July 2019. doi: 10.1109/ACCESS.2019.2926140.

[84] I. Kalyoncu, E. Ozeren, A. Burak, O. Ceylan, and Y. Gurbuz, "A Phase-calibration method for vector-sum phase shifters using a self-generated LUT," *IEEE Trans. Circuits Syst. I, Reg. Papers*, vol. 66, no. 4, pp. 1632–1642, 2019. doi: 10.1109/tcsi.2018.2885172.

[85] C. Cappellin et al., "Design of a push-broom multi-beam radiometer for future ocean observations," in *Proc. 2015 9th Eur. Conf. Antennas Propagation (EuCAP)*, Lisbon, pp. 1–5.

[86] X. Bosch-Lluis et al., "Digital beamforming analysis and performance for a digital L-band Pseudo-correlation radiometer," in *Proc. 2009 IEEE Int. Geosci. Remote Sens. Symp.*, Cape Town, pp. V-184–V-187. doi: 10.1109/IGARSS.2009.5417702.

[87] Y. Atesal, B. Cetinoneri, K. Ho, and G. Rebeiz, "A two-channel 8–20-GHz SiGe BiCMOS receiver with selectable ifs for multibeam phased-array digital beamforming applications," *IEEE Trans. Microw. Theory Techn.*, vol. 59, no. 3, pp. 716–726, 2011. doi: 10.1109/tmtt.2010.2099664.

[88] B. Yang, Z. Yu, J. Lan, R. Zhang, J. Zhou, and W. Hong, "Digital beamforming-based massive MIMO transceiver for 5G millimeter-wave communications," *IEEE Trans. Microw. Theory Techn.*, vol. 66, no. 7, pp. 3403–3418, July 2018. doi: 10.1109/TMTT.2018.2829702.

[89] F. Shigeki, "Waveguide line (in Japanese)," Japan Patent 06-053, 1994.

[90] J. Hirokawa and M. Ando, "Single-layer feed waveguide consisting of posts for plane TEM wave excitation in parallel plates," *IEEE Trans. Antennas Propag.*, vol. 46, no. 5, pp. 625–630, 1998. doi: 10.1109/8.668903.

[91] S. Shehab, N. Karmakar, and J. Walker, "Substrate-integrated-waveguide power dividers: An overview of the current technology," *IEEE Antennas Propag. Mag.*, vol. 62, no. 4, 2019. doi: 10.1109/MAP.2019.2943308.

[92] J. L. Vazquez-Roy, V. Krozer, and J. Dall, "Wideband dual-polarization microstrip patch antenna array for airborne ice sounder," *IEEE Antennas Propag. Mag.*, vol. 54, no. 4, pp. 98–107, Aug. 2012. doi: 10.1109/MAP.2012.6309160.

[93] S. S. Søbjærg, S. S. Kristensen, J. E. Balling, and N. Skou, "The airborne EMIRAD L-band radiometer system," in *Proc. 2013 IEEE Int. Geosci. Remote Sens. Symp. - IGARSS*, Melbourne, VIC, pp. 1900–1903. doi: 10.1109/IGARSS.2013.6723175.

[94] M. Zribi et al., "Combined airborne radio-instruments for ocean and land studies (CAROLS)," in *Proc. 2008 Microwave Radiometry Remote Sens. Environ.*, Firenze, pp. 1–4. doi: 10.1109/MICRAD.2008.4579471.

[95] Z. Mehrez et al., "First overview of the CAROLS measurements in September 2007," ESA. Accessed: Feb. 2021. [Online]. Available: http://earth.esa.int/workshops/smos07/pres/22_pres.pdf

[96] "Soil moisture & salinity mapping – ProSensing," Prosensing.com, 2020. Accessed: Aug. 24, 2020. [Online]. Available: https://www.prosensing.com/crb-product/plmr/

[97] J. Lian, Y. Ban, J. Zhu, J. Guo, and Z. Chen, "Planar 2-D scanning siw multibeam array with low sidelobe level for millimeter-wave applications," *IEEE Trans. Antennas Propag.*, vol. 67, no. 7, pp. 4570–4578, July 2019. doi: 10.1109/TAP.2019.2907377.

[98] J.-W. Lian, X.-Y. Zhao, Y.-L. Ban, Y. Liu, and Z. Nie, "Compact SIW 2-D butler matrix and its multibeam application," *IEEE Antennas Wireless Propag. Lett.*, vol. 20, no. 3, pp. 386–390. doi: 10.1109/LAWP.2021.3051265.

[99] Y. Yang, W. Che, W. Yang, and C. Fan," "Millimeter-wave multi-beam antenna based on 2-D SIW beam-scanning network," in *Proc. 2015 Int. Workshop on Electromagnetics: Appl. Student Innovation Competition (iWEM)*, Hsinchu, pp. 1–2. doi: 10.1109/iWEM.2015.7365050.

[100] K. S. Kona, K. Bahadori, and Y. Rahmat-Samii, "Stacked microstrip-patch arrays as alternative feeds for spaceborne reflector antennas," *IEEE Antennas Propag. Mag.*, vol. 49, no. 6, pp. 13–23, Dec. 2007. doi: 10.1109/MAP.2007.4455843.

[101] Y. Rahmat-Samii et al., "A novel lightweight dual-frequency dual-polarized sixteen-element stacked patch microstrip array antenna for soil-moisture and sea-surface-salinity missions," *IEEE Antennas Propag. Mag.*, vol. 48, no. 6, pp. 33–46, Dec. 2006. doi: 10.1109/MAP.2006.323342.

[102] S. H. Yueh, W. J. Wilson, E. Njoku, K. S. Kona, K. Bahadori, and Y. Rahmat-Samii, "Compact dual-frequency microstrip antenna feed for future soil moisture and sea surface salinity missions," in *Proc. 2003 IEEE Int. Geoscience Remote Sens. Symp. Proc. (IEEE Cat. No.03CH37477)*, Toulouse, vol. 1, pp. 497–499. doi: 10.1109/IGARSS.2003.1293821.

[103] M. Borgarino, A. Polemi, and A. Mazzanti, "Low-cost integrated microwave radiometer front-end for industrial applications," *IEEE Trans. Microw. Theory Techn.*, vol. 57, no. 12, pp. 3011–3018, Dec. 2009. doi: 10.1109/TMTT.2009.2034209.

[104] A. Alonso-Arroyo et al., "On the correlation between GNSS-R reflectivity and L-band microwave radiometry," *IEEE J. Sel. Topics Appl. Earth Observ. Remote Sens.*, vol. 9, no. 12, pp. 5862–5879, Dec. 2016. doi: 10.1109/JSTARS.2016.2588281.

GRS